MODELLING THE EFFECT OF PRESSURE ON SOOT FORMATION IN VARYING-PRESSURE COFLOW LAMINAR DIFFUSION FLAMES

By

Amin Mansouri

Bachelor of Applied Science

Isfahan University of Technology

2011

Master of Applied Science

University of Tabriz

2015

An MRP presented to Ryerson University

in partial fulfillment of the requirements for the degree of Master of Engineering in the program of Mechanical and Industrial Engineering

Author's declaration for electronic submission of an MRP

I hereby declare that I am the sole author of this MRP. This is a true copy of the MRP, including any required final revisions.

I authorize Ryerson University to lend this MRP to other institutions or individuals for the purpose of scholarly research.

I further authorize Ryerson University to reproduce this MRP by photocopying or by other means, in total or in part, at the request of other institutions or individuals for the purpose of scholarly research.

I understand that my MRP may be made electronically available to the public.

Abstract

Modelling the Effect of Pressure on Soot Formation in Varying-Pressure Coflow Laminar Diffusion Flames

Amin Mansouri

Master of Engineering, Mechanical and Industrial Engineering,
Ryerson University, 2020

Soot formation from combustion devices is a health and environmental concern. Therefore, a comprehensive understanding of soot is a necessity; however, due to its complexity, it is poorly understood, especially with high-pressure combustion. In this thesis, a detailed numerical soot formation code, CoFlame, has been successfully utilized to model varying-pressure coflow laminar diffusion flames. The results of this thesis are divided into two sections; first, an investigation of the impact of a novel pressure-based reaction rate of acetylene addition in the Hydrogen-Abstraction-Carbon-Addition (HACA) mechanism on soot formation in varying pressure flames is addressed in chapter 4. Second, an assessment of the influence of pressure on the formation of recirculation zones along the centerline of the flame and the subsequent effect of the flow field on soot formation in elevated-pressure coflow diffusion flames is addressed in chapter 5.

Acknowledgements

I would like to express my appreciation for my supervisor Professor Seth B. Dworkin. His dedication and passion were a source of inspiration coupled with invaluable guidance made this research possible and enjoyable throughout.

I would like to thank the Dworkin research group and my fellow graduate students that have provided countless hours of entertainment and with whom I have shared many experiences during my time at Ryerson University.

I would like to convey my gratitude towards my parents for their emotional support that made this academic endeavour possible.

I would like to acknowledge SciNet HPC Consortium for providing computational resources. SciNet is funded by: the Canada Foundation for Innovation under the auspices of Compute Canada; the Government of Ontario; Ontario Research Fund - Research Excellence; and the University of Toronto. I also acknowledge the Canada Research Chairs program, the Natural Sciences and Engineering Research Council of Canada, and Ryerson Faculty of Engineering and Architectural Science for financial support.

Table of Contents

List of Tables

List of Figures

Nomenclature

Latin

A	Coefficient that governs the overall fragmentation rate
As	Soot surface area per unit volume of gaseous mixture
Av	Avogadro's number
$C_C(Kn)$	Cunningham slip correction factor
C_p	Mixture specific heat capacity at constant pressure
$C_{p,k}$	Specific heat capacity of the k_{th} species
$C_{p,s}$	Specific heat capacity of soot
D	Diffusion coefficient
D_f	Fractal dimension
D_j and D_k	Diffusion coefficients for soot particles in the j_{th} and k_{th} sections
d_m	Mobility diameter
f	Volume filling factor
f_D	Transition regime correction factor
f_v	Soot volume fraction
g_z	Gravitational acceleration
h_k	Specific enthalpy of the k_{th} species
h_s	Specific enthalpy of soot
I	Spectral intensity
I_b	Spectral black-body intensity
$I_{g,i}$	Total surface growth rate of PAH condensation and HACA for the i_{th} section
$I_{ox,i}$	Oxidation rate for the i_{th} section
k_B	Boltzmann constant
KK	Total gaseous species number
l	Azimuthal angle index

m	Polar angle index
m_i	Representative mass of the i_{th} section aggregate
N_i^a	Aggerate number density
N_i^p	Soot primary particle number density
N_i	Number density of the i_{th} particle
n_p	Number of primary particles in the aggregate
p	Pressure
Q_r	Radiative heat transfer by soot, H_2O, CO_2, and CO
r	Radial position
r_A and r_B	Radii of the two colliding species
R_{abs}	Absorbing sphere cluster radius
R_f	Outer radius of an aggregate
$r_{ox,s}$	Rate of removal of soot mass due to oxidation per unit soot surface area
r_p	Primary particle radius
S_i	Fragmentation rate of the i_{th} section
T	Temperature
u	Axial velocity
v	Radial velocity
$V_{s,r}$	Soot radial diffusion velocity
$V_{s,z}$	Soot axial diffusion velocity
$V_{Ts,r}$	Radial thermophoretic velocity
$V_{Ts,z}$	Axial thermophoretic velocity
W_k	Molecular weight of the k_{th} species
W_s	Molecular weight of soot
x_i	Concentration of the i_{th} species
Y_k	Mass fraction of the k_{th} species

Y_s	Mass fraction of soot
z	Axial position

Greek

α	Surface reactivity
α	Geometric constant
β	Nucleation efficiency
$\beta_{j,k}$	Collision kernel of two aggregates in the j_{th} and k_{th} sections
$\Gamma_{i,i}$ and $\Gamma_{i,i+1}$	Breakage distribution functions
δ	Kronecker delta function
$\eta_{p,i}$	Number of primary particles per aggregate in the i_{th} section
κ	Spectral absorption coefficient
λ	Mixture thermal conductivity
λ_{mfp}	Mean free path of the gas
μ	Dynamic viscosity
μ and ξ	Directional cosines
μ_{AB}	Collisional reduced mass for the two-colliding species
$\xi_{j,k}$	Coagulation efficiency of two aggregates in the j_{th} and k_{th} sections
ρ	Mixture density
ω	Weighting function
$\dot{\omega}_k$	Production rate of the k_{th} species

Subscripts

co	Coagulation
fr	Fragmentation
nu	Nucleation
ox	Oxidation
sg	Surface growth

Acronyms

BAPYR	Benzo(a)pyrene
BAPYRS	Benzo(a)pyrenyl
BGHIF	Benzo(ghi)fluoranthene
CFD	Computational Fluid Dynamics
CHT	Conjugate Heat Transfer
CPU	Central Processing Unit
DOM	Discrete Ordinate Method (radiation model)
HACA	Hydrogen-Abstraction-Carbon-Addition
IEA	International Energy Agency
IARC	International Agency for Research on Cancer
MPI	Message Passing Interface
PAH	Polycyclic Aromatic Hydrocarbon
RTE	Radiative Transfer Equation
SIMPLE	Semi-Implicit Method for Pressure Linked Equations
TDMA	Tri-Diagonal Matrix Algorithm

Chapter 1 – Introduction

1.1 Motivation

Based on the report of the *International Energy Agency* (IEA), in 2016, Canada accounted for 2.3 percent of global total energy consumption [1]. This high quantity of energy consumption per population is due to Canada's cold climate. Although there has been some progress in using renewable energy, burning fossil fuels in furnaces and power plants is still the main source of heat and power production. Hydrocarbons are one of the most common fuels for this process. Incomplete hydrocarbon combustion leads to excess carbon and eventually generation of black carbon. Black carbon is also named soot in common vernacular. Although there is a slight difference between these two terms, in the present study the term "soot" will be used.

Soot has adverse impacts on climate change and global warming. It is the second most significant contributor to global warming after CO_2 [2]. Absorbing some sunlight and scattering the rest, soot affects ecological systems which results in global warming. It has been proven that soot has significant effects on human health, specifically on the fatality rate from cardiovascular and respiratory disease, lung cancer, and other health complications [3]. According to a recent study by *the International Agency for Research on Cancer* (IARC) on exhaust from diesel engines, soot particles mainly include polycyclic aromatic hydrocarbons (PAH), metals and inorganic salts which are detrimental for human health [4]. Accordingly, stricter regulations have been imposed on exhaust emissions of new vehicles sold in the European Union and EEA member states (e.g., EURO6 [5]). Considering these facts, mitigating soot emissions is a global concern and it is one of the essential ways to control climate change and global warming. In order to achieve these

reduced emissions, a fundamental understanding of the soot formation process is required. However, soot formation is currently poorly understood due to its complexity.

Soot formation is a complex process consisting of five main steps. These steps are PAH gas-phase growth, particle nucleation, surface growth via surface reaction (chemical) and PAH condensation (physical), particle agglomeration, and fragmentation [6]. Figure 1.1 illustrates a schematic of soot formation pathways. Soot formation begins with the decomposition of fuel into aromatic rings. These aromatic rings combine to form three-dimensional structures, which is referred to as nucleation. Nucleation is the onset of the emergence of solid soot particles from the gas-phase. These nascent particles grow via chemical reactions and physical interactions. Subsequently, they coalesce to form larger particles or coagulate to form pearl-necklace like aggregates. Surface oxidation and aggregate fragmentation compete against the growth mechanisms [7, 8].

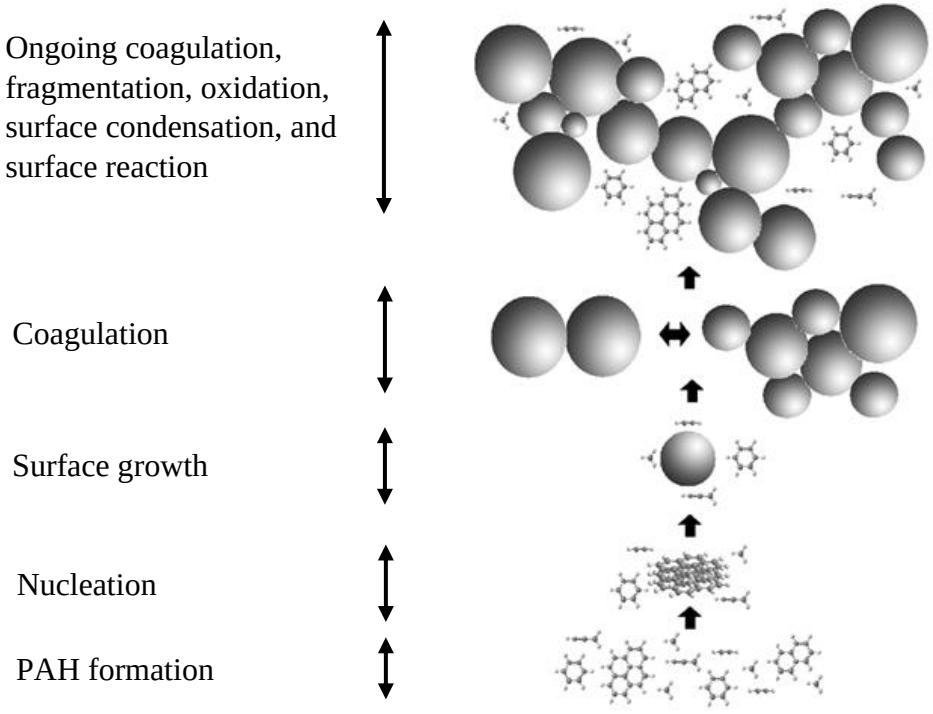

Figure 1.1: A schematic representation of the soot formation pathway

The aforementioned soot formation pathways are widely accepted by the scientific community; however, there is no consensus on the details of each process and yet there are still significant gaps in knowledge that must be filled. More details will be given in the following sections.

Soot models are divided into three categories; empirical, semi-empirical, and detailed [9]. Empirical models are the simplest ones which are based on experimental correlations for soot formation rates; however, they do not bring a detailed understanding of the soot formation and oxidation pathways. Semi-empirical models are more physically and chemically detailed than empirical ones, bringing more insights into soot formation mechanisms. The most comprehensive models are detailed soot models, which focus on the physics and chemistry of the phenomenon more than the two aforementioned model classes. Improvements in computational resources have led combustion research toward the latter model classes [9]. Overall, empirical models are more qualitative while detailed models capture soot characteristics more quantitatively.

Since most of the industrial applications of combustion occur at high pressures, it is important to understand the effect of pressure on soot formation using numerical and experimental studies. It is essential to study the effect of pressure in simplified systems such as lab flames rather than complex combustion devices, so the effects of pressure can be isolated. Due to difficulties of achieving stable flames, the number of experimental studies at elevated pressure is lower than of that at atmospheric pressure. While experimental results are difficult to interpret directly, numerical simulations can be used to better understand the effect of varying pressure on soot formation mechanisms. While experiments are still needed for validation purposes, numerical simulations give researchers more detailed information (e.g. tracking all species concentration at different points). Soot formation at higher pressures is poorly characterized and a comprehensive

study of such flames is essential. For instance, the impact of pressure on quantity of soot concentration is not fully understood. Studies by Joo and Gülder demonstrated that as pressure rises, soot concentration increases, reaches a peak and then declines monotonically [10, 11]. No thorough explanation for the impact of pressure on soot concentration existed.

1.2 Objectives

The overall objective of this research work is to broaden the knowledge base of soot formation in laminar diffusion flames. The reason to select laminar coflow diffusion flames among various configurations is due to its multidimensionality and reduced computational cost for the fluid dynamics. In this regard, by implementing soot modelling in a laminar coflow diffusion configuration, it makes assessment of soot characteristics simpler.

The first objective of this study relates to assess surface growth, and oxidation. As surface growth and oxidation, which greatly contribute to soot mass and size, are involved with surface chemical reactions to predict soot concentrations successfully, correct soot surface reaction modelling is required. A functional soot surface reactivity model proposed by Khosousi and Dworkin [12] has been examined for nine atmospheric pressure flames and successfully predicted maximum soot concentration. In spite of the capability of this functionally dependent surface reactivity in prediction of quantities and trends for soot concentration, it has never been examined for varying-pressure flames. Therefore, one of the objectives of this work is to investigate the performance of the soot surface reactivity model [12] at varying pressures to examine the possibility of altering a tuning constant with a more physically justifiable function.

As mentioned in the previous section, the impact of pressure on soot formation is poorly understood. Most of the studies conducted at high pressure demonstrated that peak soot concentration is increased with increasing pressure. However, the work by Joo and Gülder [11] has an interesting result. They showed that peak soot concentration reaches a maximum at a certain pressure and after that, it decreases monotonically with increasing pressure. Another motivating point is that at higher pressures, the experimental study [13] indicates that the entire fuel stream at 36.5 atm converted to soot. Previously, no adequate explanation for the formation of the large mass of soot existed. Therefore, the next goal of this thesis is to propose a possible reason for that unique phenomenon.

1.3 Outline of the Thesis

This thesis is outlined as follows: Chapter 2 presents a comprehensive description of the detailed computational fluid dynamics (CFD) soot formation model. Chapter 3 is a critical literature review of background information on soot characteristics, and soot formation pathways' rates. Chapter 4 investigates the validity of a soot surface reactivity model (based on temperature history) in coflow laminar diffusion flames at varying pressures. The thesis continues with the influence of pressure on the near-nozzle flow field and soot formation in laminar coflow diffusion flames in chapter 5. Finally, this thesis completes with the conclusions and recommendations for future work in chapter 6.

1.4 Author's Contribution to Collaborative Work

The work in chapter 5 is a collaborative study started by Professor Nickolas A. Eaves during his PhD under the co-supervision of Professor Murray Thomson and Professor Seth

Dworkin. The original simulations were conducted by him, followed by the first draft of the manuscript; however, it was not published. When Dr. Eaves was a postdoctoral fellow at University of Cambridge, he kindly offered the author of this thesis to work on the reviews of that article and make the manuscript stronger. One of my contributions was utilizing simulations for cold cases (flow field with no-combustion assumption) and comparing the ratios of free-stream fluid velocity near fuel tube tip to average flow velocity in cold and hot cases (flow field with combustion assumption). A comparison of the numerical and the experimental results of the radial and the axial profiles of the axial velocity for methane, ethylene, and propane flames in order to investigate the capability of the CoFlame code in capturing the recirculation zone was conducted by the author of this thesis. Finally, the work followed by adding and/or rearranging some of the arguments in the manuscript

Chapter 2 – Numerical Model

2.1 Overview

The numerical model used in this research is an in-house parallelized FORTRAN computational fluid dynamics code that includes soot particle dynamics sub-models. It was published by Eaves *et al.* [14], in which its name was given to be CoFlame thereafter. CoFlame is capable of simulating different coflow laminar diffusion flames. Figure 2.1 illustrates a schematic of a coflow laminar diffusion flame. It can be seen in Fig. 2.1 that a coflow laminar diffusion burner consists of two concentric thin-walled cylinders. The inner tube is for the fuel flow and the outer one is for the oxidizer. For different flames, burner dimension, fuel and oxidizer mass flow rates, and fuel type can be changed.

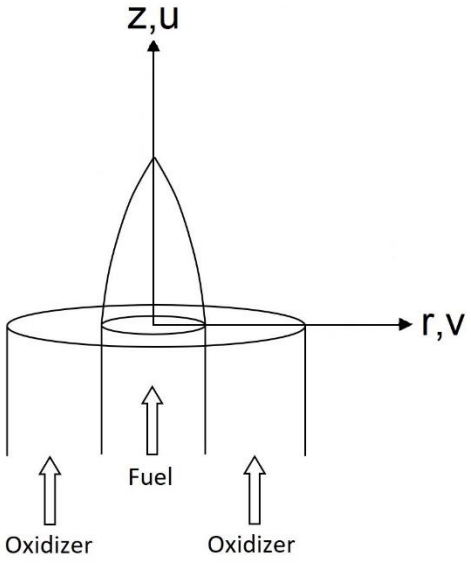

Figure 2.1: A schematic of a coflow laminar diffusion flame

Numerical simulations are conducted on several flames at varying pressures. The fuel flows for these simulations were ethylene, ethylene diluted with nitrogen, and ethane [15-17]. Further

details about the burner dimensions, fuel and oxidizer mass flow rates, and numerical domains of these flames are addressed separately in subsequent chapters. All the information in this chapter is more generic in that it is common to all flames simulated in the present thesis.

2.2 Governing Equations

For the gaseous phase, CoFlame solves fully coupled conservation equations for mass, momentum, energy, and species mass fraction. The equations are solved in a two-dimensional (*r* and *z*) axi-symmetrical cylindrical co-ordinate system wherein *r* represents the radial and *z* is the axial co-ordinates. The following equations are the same as in previous studies [12, 14, 18-29].

Conservation of mass:

$$\frac{1}{r}\frac{\partial}{\partial r}(r\rho v)+\frac{\partial}{\partial z}(\rho u)=0. \tag{1}$$

Conservation of axial momentum:

$$\begin{aligned}\rho v\frac{\partial u}{\partial r}+\rho u\frac{\partial u}{\partial z}=&-\frac{\partial p}{\partial z}+\frac{1}{r}\frac{\partial}{\partial r}\left(r\mu\frac{\partial u}{\partial r}\right)+2\frac{\partial}{\partial z}\left(\mu\frac{\partial u}{\partial z}\right)\\&-\frac{2}{3}\frac{\partial}{\partial z}\left[\frac{\mu}{r}\frac{\partial}{\partial r}(rv)\right]-\frac{2}{3}\frac{\partial}{\partial z}\left(\mu\frac{\partial u}{\partial z}\right)+\frac{1}{r}\frac{\partial}{\partial r}\left(r\mu\frac{\partial v}{\partial z}\right)+\rho g_z.\end{aligned} \tag{2}$$

Conservation of radial momentum:

$$\begin{aligned}\rho v\frac{\partial v}{\partial r}+\rho u\frac{\partial v}{\partial z}=&-\frac{\partial p}{\partial r}+\frac{2}{r}\frac{\partial}{\partial r}\left(r\mu\frac{\partial v}{\partial r}\right)+\frac{\partial}{\partial z}\left(\mu\frac{\partial v}{\partial z}\right)-\frac{2}{3}\frac{1}{r}\frac{\partial}{\partial r}\left[\mu\frac{\partial}{\partial r}(rv)\right]\\&-\frac{2}{3}\frac{1}{r}\frac{\partial}{\partial r}\left(r\mu\frac{\partial u}{\partial z}\right)+\frac{\partial}{\partial z}\left(\mu\frac{\partial u}{\partial r}\right)-\frac{2\mu v}{r^2}+\frac{2}{3}\frac{\mu}{r^2}\frac{\partial}{\partial r}(rv)+\frac{2}{3}\frac{\mu}{r}\frac{\partial u}{\partial z}.\end{aligned} \tag{3}$$

Conservation of energy:

$$C_p\left(\rho v\frac{\partial T}{\partial r}+\rho u\frac{\partial T}{\partial z}\right)=\frac{1}{r}\frac{\partial}{\partial r}\left(r\lambda\frac{\partial T}{\partial r}\right)+\frac{\partial}{\partial z}\left(\lambda\frac{\partial T}{\partial z}\right)-\sum_{k=1}^{KK}h_k W_k\dot{\omega}_k$$
$$-\sum_{k=1}^{KK}\left[\rho C_{p,k}Y_k\left(V_{k,r}\frac{\partial T}{\partial r}+V_{k,z}\frac{\partial T}{\partial z}\right)\right] \quad (4)$$
$$-\rho C_{p,s}Y_s\left(V_{s,r}\frac{\partial T}{\partial r}+V_{s,z}\frac{\partial T}{\partial z}\right)-h_s W_s\dot{\omega}_s+Q_r.$$

Conservation of species mass fractions:

$$\rho v\frac{\partial Y_k}{\partial r}+\rho u\frac{\partial Y_k}{\partial z}=-\frac{1}{r}\frac{\partial}{\partial r}\left(r\rho Y_k V_{k,r}\right)-\frac{\partial}{\partial z}\left(\rho Y_k V_{k,z}\right)+W_k\dot{\omega}_k \quad (k=1, 2, ..., KK). \quad (5)$$

In equations (1) to (5), u is the axial velocity, v is the radial velocity, ρ is the mixture density, μ is the dynamic viscosity, g_z is the acceleration due to gravity in the axial direction, is the k_{th} species mass fraction, KK is the number of species which in the present model is 94, $V_{k,r}$ and $V_{k,z}$ are the k_{th} species radial and axial diffusion velocities respectively, W_k is the molecular weight of the k_{th} species, $\dot{\omega}_k$ is the production rate of the k_{th} species due to gas phase chemical reaction and interactions with the solid soot phase, C_p is the mixture specific heat capacity at constant pressure, T is the temperature, λ is the mixture thermal conductivity, h_k is the specific enthalpy of the k_{th} species, $C_{p,k}$ is the specific heat capacity of the k_{th} species at constant pressure, $C_{p,s}$ is the specific heat capacity of soot at constant pressure (assumed to be the same as graphite), Y_s is the soot mass fraction, $V_{s,r}$ and $V_{s,z}$ are the soot radial and axial diffusion velocities respectively, h_s is the specific enthalpy of soot (assumed to be the same as graphite), W_s is the molecular weight of soot (assumed to be the same as carbon), and Q_r is the radiative heat transfer by soot, H_2O, CO_2, and CO.

Additionally, a fixed soot sectional model has been included in CoFlame in which soot particle mass is divided logarithmically into thirty-five sections [14]. Each section has a fixed prescribed mass. Since nucleation is the first step in soot formation, the nascent soot primary particles only occupy the first section. The impact of nucleation on the other of thirty-four sections is zero. By surface growth and coagulation, particles migrate from the lower sections to higher ones. Conversely, particles move from higher sections to lower ones when oxidation or fragmentation occurs. For each section, two transport equations are solved, which are soot primary particle number density (N_i^p) and soot aggregate number density (N_i^a), where $i = 1, 2, ..., 35$ is the section number [14].

Conservation of soot primary particle number density:

$$\rho v\frac{\partial N_i^p}{\partial r}+\rho u\frac{\partial N_i^p}{\partial z}=\frac{1}{r}\frac{\partial}{\partial r}\left(r\rho D_i^a\frac{\partial N_i^p}{\partial r}\right)+\frac{\partial}{\partial z}\left(\rho D_i^a\frac{\partial N_i^p}{\partial z}\right)$$
$$-\frac{1}{r}\frac{\partial}{\partial r}\left(r\rho N_i^p V_{Ts,r}\right)-\frac{\partial}{\partial z}\left(\rho N_i^p V_{Ts,z}\right) \quad (6)$$
$$+\rho\left(\left.\frac{\partial N_i^p}{\partial t}\right|_{nu}+\left.\frac{\partial N_i^p}{\partial t}\right|_{co}+\left.\frac{\partial N_i^p}{\partial t}\right|_{sg}+\left.\frac{\partial N_i^p}{\partial t}\right|_{ox}+\left.\frac{\partial N_i^p}{\partial t}\right|_{fr}\right).$$

Conservation of soot aggregate number density:

$$\rho v\frac{\partial N_i^a}{\partial r}+\rho u\frac{\partial N_i^a}{\partial z}=\frac{1}{r}\frac{\partial}{\partial r}\left(r\rho D_i^a\frac{\partial N_i^a}{\partial r}\right)+\frac{\partial}{\partial z}\left(\rho D_i^a\frac{\partial N_i^a}{\partial z}\right)$$
$$-\frac{1}{r}\frac{\partial}{\partial r}\left(r\rho N_i^a V_{Ts,r}\right)-\frac{\partial}{\partial z}\left(\rho N_i^a V_{Ts,z}\right) \quad (7)$$
$$+\rho\left(\left.\frac{\partial N_i^a}{\partial t}\right|_{nu}+\left.\frac{\partial N_i^a}{\partial t}\right|_{co}+\left.\frac{\partial N_i^a}{\partial t}\right|_{sg}+\left.\frac{\partial N_i^a}{\partial t}\right|_{ox}+\left.\frac{\partial N_i^a}{\partial t}\right|_{fr}\right).$$

where D_i^a is the particle diffusion, and $V_{Ts,r}$ and $V_{Ts,z}$ are radial and axial thermophoresis velocities respectively. The soot sectional model comprises various processes including nucleation (*nu*), coagulation (*co*), PAH condensation and Hydrogen-Abstraction-Carbon-Addition (HACA) surface growth (*sg*), surface oxidation (*ox*), and fragmentation (*fr*). In order to solve the number density transport equations, several rates are needed. Further details for calculation of these rates will be addressed more thoroughly in the next chapter.

Thermophoresis is a phenomenon seen in a mixture of mobile particles. It is a force due to the temperature gradient between hot and cold particles and causes hotter particles to move in the direction of colder particles. Thermophoretic velocities need to be calculated to take this phenomenon into account. The equation for calculating thermophoretic velocities is as follows [30]:

$$V_{Ts,x_i} = -0.55 \frac{\mu}{\rho T} \frac{\partial T}{\partial x_i} \quad (x_i = r,\ z). \tag{8}$$

2.3 Radiation Model

The radiation model incorporated in CoFlame uses the discrete ordinates method (DOM) coupled with the statistical narrow-band correlated-*k*-based model to calculate radiative heat transfer by soot, H_2O, CO_2, and CO [31]. The radiative transfer equation (RTE) is integrated with DOM along a prescribed number of discrete ordinates. Below, the discretized RTE is presented in cylindrical co-ordinates [32]:

$$-\kappa I_{m,l} + \kappa I_b = \frac{\mu_{m,l}}{r} \frac{\partial r I_{m,l}}{\partial r} + \xi_{m,l} \frac{\partial I_{m,l}}{\partial z} - \frac{1}{r} \left(\frac{\alpha_{m,l+\frac{1}{2}} I_{m,l+\frac{1}{2}} - \alpha_{m,l-\frac{1}{2}} I_{m,l-\frac{1}{2}}}{\omega_{m,l}} \right). \tag{9}$$

where m is the polar angle index from 1 to M (based on the number of ordinates selected), l is the azimuthal angle index from 1 to L(m), μ and ξ are directional cosines, κ is the spectral absorption coefficient, I is the spectral intensity, I_b is the spectral black-body intensity, α is a geometric constant [32], ω is a weighting function associated with the direction defined by (m,l). The set of discrete ordinates is defined using T_3 quadrature for an axisymmetric cylinder [33]. Further details on validation of the original DOM can be found in [34, 35].

2.4 Boundary Conditions

The boundary conditions are the same as previous studies [12, 14, 18-29]. Figure 2.2 illustrates a schematic of boundary conditions on a coflow co-annular burner employed in the CoFlame code, using a top-hat velocity on the inlet, a symmetry condition on the central axis, free-slip conditions on the outer radial boundary, and zero-gradient conditions on the outflow.

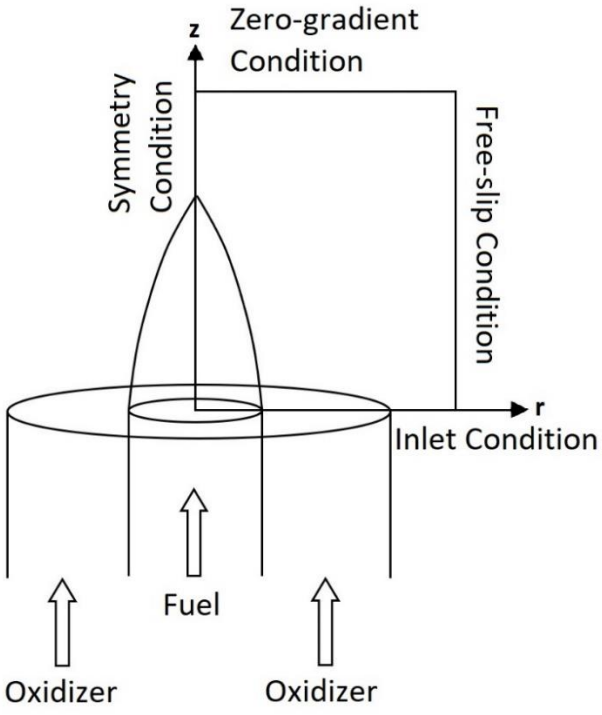

Figure 2.2: A schematic of a coflow burner with boundary conditions present

Boundary conditions are given by:

Inlet:

Inlet velocities are assumed to have a top-hat profile as results are insensitive to the choice of the velocity profile (top-hat or parabolic) [21]:

$$\begin{aligned} &u = u_{fuel},\ \ Y_{fuel} = 1.0 && r \le r_i \\ &u = 0,\ \ \ Y_k = 0 && r_i \le r \le r_o \\ &u = u_{air},\ \ Y_{O_2} = 0.231, Y_{N_2} = 0.769 && r \ge r_o \\ &v = 0,\ \ N_i^a = 0,\ \ N_i^p = 0,\ \ T = 300K \end{aligned} \tag{10}$$

Axis of symmetry:

Zero-gradient conditions are applied on the axis of symmetry as below:

$$\frac{\partial u}{\partial r} = 0,\ \ v = 0,\ \ \frac{\partial T}{\partial r} = 0,\ \ \frac{\partial Y_k}{\partial r} = 0,\ \ \frac{\partial N_i^a}{\partial r} = 0,\ \ \frac{\partial N_i^p}{\partial r} = 0 \tag{11}$$

Outer radial boundary:

Zero-gradient conditions and species mass fractions of ambient air are applied at the outer radial boundary as below:

$$\frac{\partial u}{\partial r} = 0,\ \ v = 0,\ \ \frac{\partial T}{\partial r} = 0,\ \ Y_{O_2} = 0.231,\ \ Y_{N_2} = 0.769,\ \ \frac{\partial N_i^a}{\partial r} = 0,\ \ \frac{\partial N_i^p}{\partial r} = 0 \tag{12}$$

Outflow:

Zero-gradient conditions are applied for the outflow as below:

$$\dot{m}_{outflow} = \dot{m}_{inlet},\ \ \frac{\partial v}{\partial z} = 0,\ \ \frac{\partial T}{\partial z} = 0,\ \ \frac{\partial Y_k}{\partial z} = 0,\ \ \frac{\partial N_i^a}{\partial z} = 0,\ \ \frac{\partial N_i^p}{\partial z} = 0 \tag{13}$$

2.5 Numerical Method

As stated earlier in this chapter, all the information given in this chapter is that which is applicable to all simulations. Therefore, details about dimensions of the computational domain, control volumes, and other such details are given separately in their respective chapters. It also should be noted that, due to the computationally intense nature of the simulations, a mesh sensitivity analysis was not carried out in a classical manner in which the computational domain is held constant while the number of control volumes is increased to reach a grid-independent solution. Additionally, given past experiences with the code and mesh independence studies [14], while the quantitative results may slightly change as the mesh is refined, qualitative trends typically stay the same. Eaves *et al.* [14] demonstrated that when a halving of the spacing in both coordinate directions is performed, the change in the all soot parameters is less than 10% for the simulated flames. This variation seems reasonable since the uncertainty for soot concentration in experimental studies is around 40% [15, 36].

The governing equations are discretized by using the finite volume method in the same manner as previous works [12, 18-22, 24, 29]. For convective terms, power law schemes are used for discretization, while a second-order difference scheme is used to discretize diffusive terms [37]. To handle the pressure and velocity coupling, the Semi-Implicit Method for Pressure Linked Equations (SIMPLE algorithm) is implemented [37]. A staggered mesh is used to solve governing equations at each pseudo-time interval. The thermal properties of the gaseous species and chemical reaction rates are provided by CHEMKIN subroutines [38, 39].

Figure 2.3 represents the numerical procedure implemented in the CoFlame code to solve the governing of equations. An arbitrary initial guess is required for solving the velocity and

temperature fields, mole fraction, and other variables. The initial guess has a strong influence on the convergence time. Pseudo-transient continuation is employed for obtaining a converged solution from an initial guess. After calculating the thermal properties and transport data, the numerical procedure starts by solving momentum and the pressure correction equations at each pseudo-time step. Then, the gaseous species governing equations are solved for each control volume instantaneously to manage the stiffness of the problem and accelerate the convergence. Afterwards, the conservation equations of soot primary particle number density and soot aggregate number density are solved simultaneously for each control volume. The soot sectional conservation equations are solved control-volume-by-control-volume consecutively for the whole domain.

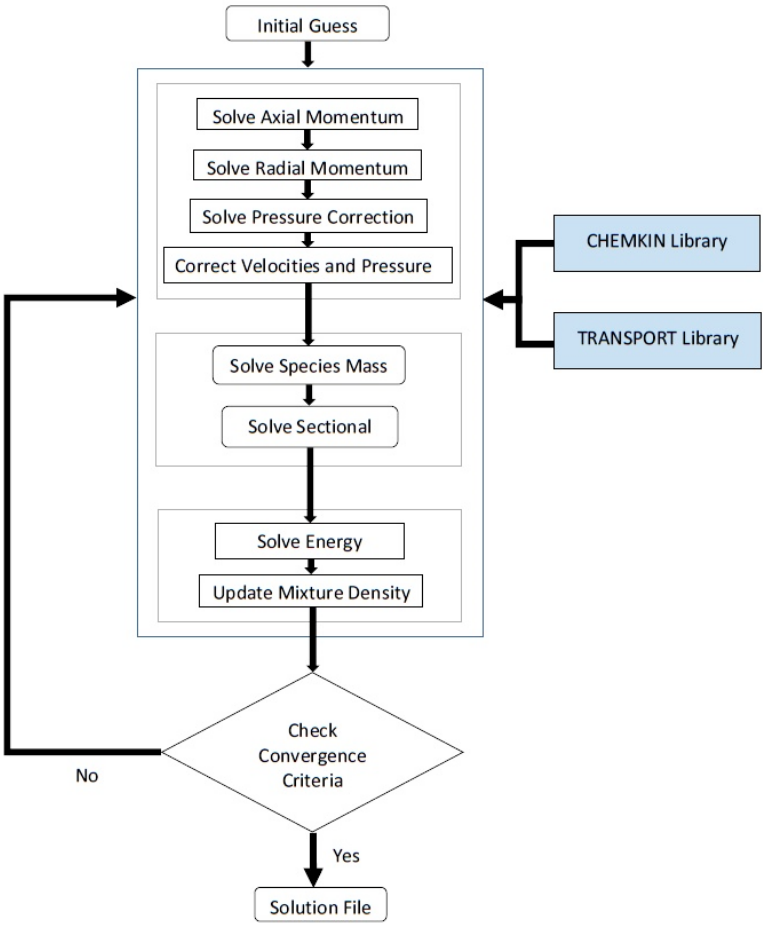

Figure 2.3: Numerical procedure of the CoFlame code

The next step is to solve the energy equation to obtain an updated temperature field. Momentum, pressure correction and energy equations are solved using a modified Tri-Diagonal Matrix Algorithm (TDMA) suitable for pentadiagonal matrices that is an iterative procedure. At the end of each iteration, the updated mixture density is provided, and a convergence check is performed. If the maximum relative error for the flame temperature, soot volume fraction, and species concentrations becomes less than the convergence criterion, 1×10^{-3}, the solution is deemed converged. Otherwise, the next iteration starts, and the process continues until the maximum relative error satisfies the convergence limit. Due to the computational intensity, parallelization methods have been employed to accelerate the calculations.

2.6 Parallelization Strategy

Due to the computational intensity of the problem, obtaining solution with serial processing is time-consuming and parallelization techniques have been employed. Message Passing Interface (MPI) has been used in the CoFlame code as a parallel programming tool due to its ease of use [40]. A Domain Decomposition Method (DDM) has been incorporated in such a way that the computational domain is divided into N_p sub-domains, in which N_p is the total number of processes [41]. Each process or sub-domain is assigned to a processor. Each processor solves the governing equations for a smaller number of control volumes and all processors work simultaneously. Therefore, parallelization speeds up the calculations.

There are different ways to divide the computational domain. It can be decomposed only in one direction (i.e. either in the radial or in the axial direction) or in both radial and axial directions. A parallel code with a well-decomposed domain needs minor adjustments when a different mesh is employed. Also, the smaller the length of the overlapping boundaries of the sub-

domains, the fewer repeated calculations occur for same nodal points. Zhang *et al.* [20] demonstrated that decomposing the computational domain in two directions is not as flexible as only in one direction. When different meshes are employed, the computational domain has to be re-decomposed in two directions. Also, variables and arrays related to both radial and axial directions have to be re-defined. It was also shown that domain decomposition in the radial direction imposes larger length of the overlapping boundaries of the sub-domains compared to with the axial direction. To further visually expand the argument, comparing the length of the domain along the axial direction to that along the radial direction would be beneficial. Figure 2.4 represents a temperature profile with the mesh displayed for an ethylene flame diluted with nitrogen at 8 bars. It is noteworthy that this flame has not been chosen from one of the simulated flames in this thesis to ensure that this is as an unbiased example and any other flames can be selected. Further details about the flame and burner configuration or the dilution ratio are not the subjects of interest; however, they can be found in [16].

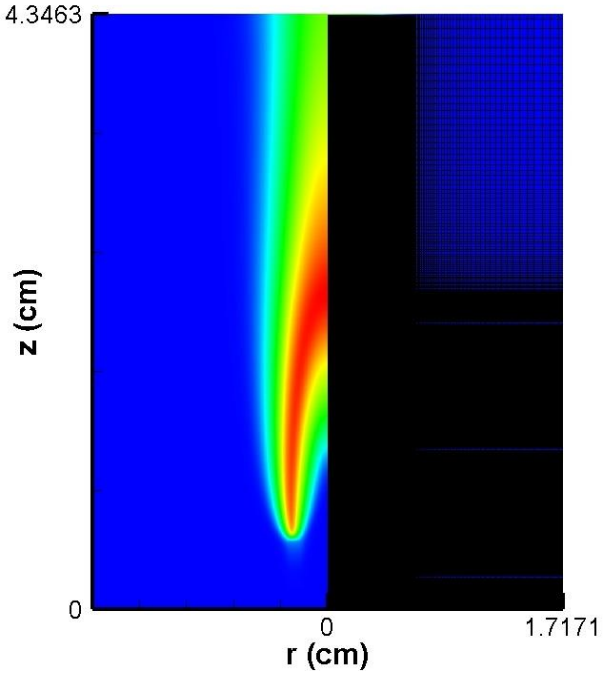

Figure 2.4: An example of the computational domain with the mesh on the right side.

The computational domain is formed as an axy-symmetric grid, with 400 control volumes in the axial and 190 in the radial directions. The length of the domain along the axial direction is 4.3463 cm and the length of the domain along the radial direction is 1.7171 cm. A simple calculation shows that the length of the overlapping region when domain decomposition is only in the radial direction is 825.80 cm, while this length for decomposition only in the axial direction is 686.84 cm. Therefore, in the present study, the computational domain is decomposed into N_p sub-domains in the axial direction.

2.7 Summary

In this chapter, the numerical model, CoFlame code, utilized in this study had been described in detail. First, the gaseous phase governing equations were addressed, followed by boundary conditions. This chapter continued by explaining the structure of the CoFlame code, and finally it concluded with the parallelization strategy used in the code. In the next chapter, soot formation and decomposition sub-models are explained in detail.

Chapter 3 – Soot Formation Theory

3.1 Overview

Soot particles are products of pyrolysis of a parent fuel in fuel-rich conditions. They are generated in laminar diffusion [9, 42-49], laminar premixed [4, 50-53], and turbulent [54-57] flames. As mentioned in chapter 1, soot formation starts with the fuel decomposition into small molecules which form PAHs. This process ultimately leads to nucleation which is the first step in formation of nascent soot particles. These nascent soot particles are approximately spherical with the diameter range of 1-5 nm [58].

As nascent soot particles collide with each other, with continuous coagulation of these nanoparticles, as well as surface reactions and condensation, mature soot particles are formed [59]. The size range of mature soot particles is generally from 20 to 60 nm [60]. The term “soot primary particle” is typically used for spherical building block components of both nascent and mature particles regardless of the size range. Soot primary particles aggregate and grow together. Fractal-like soot aggregates consist of approximately equally-sized spherical primary particles with a fractal dimension being approximately $D_f = 1.8$ for both laminar [61] and turbulent flames [62]. Lastly, soot particles lose mass via oxidation and fragmentation. Most of these mechanisms occur simultaneously throughout the entire flame. In the following sections, the soot sub-models incorporated in the present CFD model are addressed in further details.

3.2 Gas-Phase Chemistry

In all combustion processes, understanding of chemical reactions is essential. In fuel-rich combustion, the ratio of oxidizer to fuel is lower than that stoichiometric mixtures which results in remaining excessive carbon and eventually formation of soot molecules. Moreover, fuel decomposition at high temperature involves many sequential reactions containing several intermediate species such as C_2H_2, C_4H_i, C_5H_5, and CH_3 that form aromatic rings that are hypothetically considered as soot precursors [63-65]. Thus, one of the significant elements of numerical soot simulations is an adequate chemical kinetic mechanism for the fuel being investigated.

There are several chemical kinetic mechanisms which can be used as libraries of reactions in combustion modelling, in the current literature. For instance, GRI-Mech 3.0 is an optimized mechanism for modelling natural gas combustion [66]. Each mechanism has its own benefits and drawbacks. Some are more detailed and give more accurate results; some have fewer intermediate species or reactions at the cost of accuracy. A study by Dworkin *et al.* [21] compared the chemical kinetic mechanism presented by Slavinskaya and Frank [67] with two other mechanisms described by Appel *et al.* [8], and Marinov *et al.* [68] based on PAH growth mechanisms in an ethylene-air coflow laminar diffusion flame. According to [21], in spite of the similar fuel oxidation chemistry in these three mechanisms, the PAH growth pathways vary significantly. While two [8, 67] of the three mechanisms are capable of well characterizing soot concentration along the wing regions of the flame, only the mechanism described by Slavinskaya and Frank [67] with modifications in the PAH growth pathways [18, 21] is able to predict the correct order of magnitude for soot concentration along the centerline of the flame.

The semi-detailed mechanism in [18] contains 93 species and 729 reactions and is based on C_0-C_2 chemistry, and can predict the formation of PAHs up to five aromatic rings (A_5). The kinetic model comprises of three sub-mechanisms including methane oxidation, ethylene oxidation, and the formation of PAHs up to five-ring molecules. In order to reduce the number of global reactions, some of the multistep reactions in the PAH growth routes, such as diacetylene addition, were lumped together. This mechanism has been validated for atmospheric and high-pressure flames [22, 67]. Therefore, the chemical kinetic mechanism used in this thesis is the same as in [18]; however, the CoFlame code is compatible with all mechanisms as well [14].

3.3 Soot Nucleation

Soot nucleation, which is also referred to as “inception”, is the first step in the generation of soot particles. This process is the transition from gas-phase carbon matter to nascent solid soot particles. Although the mechanisms for soot nucleation are not fully characterized, there are some hypotheses in the literature. Three main pathways have been proposed that are responsible for particle inception [69]. The first proposed pathway is through growing two-dimensional PAHs into fullerene-like structures [70]. The other two pathways are through the physical and chemical coalescence of PAHs into formation of three-dimensional structures. Since the first pathway relies on surface growth, which is too slow to account for particle inception rates [71, 72], it alone cannot be responsible for all soot nucleation [69]. The other two routes are not necessarily mutually exclusive, and a study conducted by D’Anna [73] demonstrated that the relative ratio between these two mechanisms is defined based on the temperature and radical populations.

The contribution of each pathway to soot nucleation is unknown due to the complex nature of this phenomenon. Numerical models mostly prescribe nucleation to occur via only PAH

dimerization in a free molecular collision regime [71]. Both PAH dimerization and growth pathways contribute to the formation of multi-ringed aromatic molecules. In the presence of large PAHs, the first condensed-phase materials emerge. After dehydrogenation and additional mass growth, condensed particles convert to nascent solid soot particles. In the present thesis, it is assumed that 0.01% of PAHs bond together after colliding. The governing equation for dimerization of two colliding species in the present nucleation model is as follows [28].

$$\left.\frac{\partial N_1^a}{\partial t}\right|_{nu} = \left.\frac{\partial N_1^p}{\partial t}\right|_{nu} = \beta\sqrt{\frac{8\pi k_B T}{\mu_{AB}}}(r_A + r_B)^2 Av^2[A][B]$$
$$\left.\frac{\partial N_i^a}{\partial t}\right|_{nu} = \left.\frac{\partial N_i^p}{\partial t}\right|_{nu} = 0, \quad i = 2, 3, ..., 35 \tag{1}$$

where β is the nucleation efficiency and is set to 0.0001, k_B is the Boltzmann constant, Av is Avogadro's number, μ_{AB} is the collisional reduced mass for the two colliding PAHs, r_A and r_B are the radii of the two colliding PAHs, and $[A]$ and $[B]$ are the concentrations of the two colliding PAHs [28]. The collisional reduced mass converts two PAHs into one species with an equivalent mass. For modelling purposes, based on the study conducted by Saffaripour *et al.* [28], three presumed species contributing to the PAH dimerization in soot nucleation are benzo(a)pyrene (BAPYR), benzo(a)pyrenyl (BAPYRS), and benzo(ghi)fluoranthene (BGHIF).

3.4 Coagulation

Soot particles collide with each other to form aggregates. Due to the random motion of primary particles, they undergo many collisions to eventually, under the right conditions, aggregate with each other. It is assumed that for all Knudsen numbers, the coagulation source terms are calculated based on the collision kernel of soot aggregates. The Knudsen number is a

dimensionless number defined as the ratio of the molecular mean free path length to a representative physical length scale, and it helps to determine whether continuum mechanics or statistical mechanics uses in modelling. If the Knudsen number is a very small number, continuum mechanics is an acceptable assumption, while for the numbers near or greater than unity, statistical mechanics should be used. The governing equations of coagulation rates for aggregates and primary particles are given as below [74-77].

$$\left.\frac{\partial N_i^a}{\partial t}\right|_{co} = \sum_{m_{i-1}\le m_j+m_k\le m_{i+1}}^{k\le j\le i}\left(1-\frac{\delta_{j,k}}{2}\right)\eta\beta_{j,k}\xi_{j,k}N_j^aN_k^a - N_i^a\sum_{k=1}^{35}\beta_{i,k}\xi_{i,k}N_k^a \tag{2}$$

$$\left.\frac{\partial N_i^p}{\partial t}\right|_{co} = \sum_{m_{i-1}\le m_j+m_k\le m_{i+1}}^{k\le j\le i}\left(1-\frac{\delta_{j,k}}{2}\right)\eta\eta_p\beta_{j,k}\xi_{j,k}N_j^aN_k^a - \eta_{p,i}N_i^a\sum_{k=1}^{35}\beta_{i,k}\xi_{i,k}N_k^a \tag{3}$$

where m_i is the representative mass of the i_{th} section aggregate, δ is the Kronecker delta function, $\beta_{j,k}$ is the collision kernel of two aggregates in the j_{th} and k_{th} sections, $\eta_{p,i}$ is the number of primary particles per aggregate in the i_{th} section, and $\xi_{j,k}$ is the coagulation efficiency of two aggregates in the j_{th} and k_{th} sections. Coagulation efficiency is set to 0.20 in this work [78]. After coagulation of the masses of the j_{th} and k_{th} sections, η is a parameter to ensure the mass and number of aggregates are conserved by weighting the newly formed mass into two adjacent sections. The equation for η is given as follows [14].

$$\eta = \begin{cases} \dfrac{m_{i+1}-(m_j+m_k)}{m_{i+1}-m_i} & if\ m_i \le m_j+m_k \le m_{i+1} \\ \dfrac{m_{i-1}-(m_j+m_k)}{m_{i-1}-m_i} & if\ m_{i-1} \le m_j+m_k \le m_i \end{cases} \tag{4}$$

Furthermore, to ensure that the primary particle size and number are conserved after coagulation, a factor η_p is defined to weight primary particles into two adjacent sections and is calculated as below [14].

$$\eta_p = \frac{m_i}{m_j + m_k}(\eta_{p,j} + \eta_{p,i}) \tag{5}$$

Also, the collision kernel, $\beta_{j,k}$, is calculated as [79]:

$$\beta_{j,k} = 4\pi R_{abs}(D_j + D_k) f_D \tag{6}$$

where R_{abs} is the absorbing sphere cluster radius, D_j and D_k are the diffusion coefficients for soot particles in the j_{th} and k_{th} sections, and f_D is the transition regime correction factor. The diffusion coefficient for soot particles, D, is calculated as:

$$D = \frac{k_B T C_C(Kn)}{3\pi\mu d_m} \tag{7}$$

where k_B is the Boltzmann constant, T is the gas temperature, μ is the gas viscosity, d_m is the mobility diameter, $C_C\,(Kn)$ is the Cunningham slip correction factor as a function of the Knudsen number Kn, and is given by [80]:

$$C_C(Kn) = 1 + 1.612Kn \tag{8}$$

where the Knudsen number, Kn, is defined as:

$$Kn = \frac{2\lambda_{mfp}}{d_m} \tag{9}$$

where λ_{mfp} is the mean free path of the gas, which is assumed to be the same as the mean free path of air, and d_m is the mobility diameter of the soot aggregate and is calculated as:

$$d_m = \begin{cases} 2r_p n_p^{0.43} & \textit{free molecular regime} \\ 2R_f \left(\frac{D_f - 1}{2} \right)^{0.7} & \textit{continuum regime} \end{cases} \tag{10}$$

where r_p is the primary particle radius, n_p is the number of primary particles in the aggregate, D_f is the fractal dimension, and R_f is the outer radius of an aggregate which is given by:

$$R_f = r_p (f n_p)^{1/D_f} \tag{11}$$

where f is the volume filling factor and according to Naumann [81] it is set to 1.43.

In Eq. (6), f_D, which is referred to as the transition regime correction factor, is calculated by using a simple approximation of flux-matching theory and is given by:

$$f_D = \frac{1 + Kn_D}{1 + 2Kn_D(1 + Kn_D)} \tag{12}$$

where Kn_D is the diffusion Knudsen number, which describes the transition between continuum and free molecular diffusion and is given by:

$$Kn_D = \frac{\lambda_{mfp,12}}{R_{abs}} \tag{13}$$

where $\lambda_{mfp,12}$ is the diffusion mean free path and is given by:

$$\lambda_{mfp,12} = \frac{D_j + D_k}{\sqrt{\frac{2k_B T}{\pi}\left(\frac{1}{m_j} + \frac{1}{m_k}\right)}} \tag{14}$$

where m_j and m_k are the masses of soot aggregates in the j_{th} and k_{th} sections respectively.

3.5 Soot Surface Reactions

Soot primary particles grow via PAH condensation, which relies on physical PAH bonds. On the contrary, soot primary particles can reduce in size by surface oxidation from OH and O_2. Surface oxidation from OH occurs in fuel-rich regions, while O_2 oxidation is dominant in fuel-lean conditions [14]. PAH condensation is modeled utilizing transition and continuum regime collision theory between PAHs and soot aggregates.

The HACA-based surface growth and oxidation scheme in the present model has been developed by Frenklach and coworkers [8, 72]. This scheme which includes six surface reactions is addressed in Table 1. Unlike PAH condensation, the reaction of soot with OH radicals (Reaction No. 6) is based on the free molecular regime collision theory. The collision efficiency of soot molecules and OH radicals in the present model is 0.13 [44]. The kinetics of other surface reactions (Reactions No. 1 to 5) are characterized using the concept of soot surface sites which either are saturated $(C_{soot} - H)$ or dehydrogenated $(C_{soot} \cdot)$.

Table 3.1: HACA-based soot surface growth and oxidation reactions [8]

No.	**Reaction**	**A** $(cm^3\ mol^{-1}\ S^{-1})$	**b**	**E_a** **(kcal / mol)**
1	$C_{soot} - H + H \rightleftharpoons C_{soot} \cdot + H_2$	4.2×10^{13}	0.0	13.0
2	$C_{soot} - H + OH \rightleftharpoons C_{soot} \cdot + H_2O$	1.0×10^{10}	0.73	1.43
3	$C_{soot} \cdot + H \rightarrow C_{soot} - H$	2.0×10^{13}	0.0	0.0
4	$C_{soot} \cdot + C_2H_2 \rightarrow C_{soot} - H + H$	8.0×10^{7}	1.56	3.8
5	$C_{soot} \cdot + O_2 \rightarrow 2CO + product$	2.2×10^{12}	0.0	7.5
6	$C_{soot} - H + OH \rightarrow CO + product$		$\gamma_{OH} = 0.13$	

To obtain the reaction rates, the concentration of total surface sites for section *i* which is simply the sum of concentrations of saturated and dehydrogenated surface sites is required.

$$[C_{soot} - T]_i = \frac{\chi C_{soot-H} A_{s,i} N_i}{A_v} \tag{15}$$

where χC_{soot-H} is the number of sites per unit soot surface area and is set to a constant quantity of 2.3×10^{15} sites/cm^2 [72], $A_{s,i}$ is the surface area of soot particles in the i_{th} section, and N_i is the number of soot particles in the i_{th} section. The relationship between saturated and dehydrogenated sites is obtained from a steady state approximation and it is given by:

$$[C_{soot}\cdot]_i = [C_{soot} - H]_i \times \frac{(k_1\chi_H + k_2\chi_{OH})}{k_{-1}\chi_{H_2} + k_{-2}\chi_{H_2O} + k_4\chi_{C_2H_2} + k_5\chi_{O_2} + k_1\chi_H + k_2\chi_{OH}} \tag{16}$$

where $\chi_{H_2}, \chi_{H_2O}, \chi_{C_2H_2}, \chi_{O_2}, \chi_H, \chi_{OH}$ are mole fractions, and k_i is the forward pre-site rate coefficient for the i_{th} reaction where $i = 1, 2, 3, 4, 5$, and k_{-j} is the reverse pre-site rate coefficient for the j_{th} reaction, where $j = 1, 2$. It should be noted that only the first two reactions in Table 1 are reversible while the rest are irreversible. Equation (16) is a modified version of the original formulation [8, 72] in a manner that the fractional term does not exceed unity. Therefore, the concentration of saturated sites can be calculated from the subtraction of the concentration of dehydrogenated sites from the total concentration.

In the present soot sectional model, particles are assigned to different sections according to their masses. The source terms due to surface growth are obtained using a method referred to as the “three-point method” which conserves particle number density and mass [82]. It is called the

three-point method because N_i depends on the variables of the sections i-1, i, and i+1 [82]. The source terms for aggregates and primary particles in the i_{th} section are as follows:

$$\left.\frac{\partial N_i^a}{\partial t}\right|_{sg} = \begin{cases} -\dfrac{I_{g,i}}{m_{i+1}-m_i} & if\ \ i=1 \\ \dfrac{I_{g,i-1}}{m_i-m_{i-1}} - \dfrac{I_{g,i}}{m_{i+1}-m_i} & if\ \ i=2,\ldots,\ SN-1 \\ \dfrac{I_{g,i-1}}{m_i-m_{i-1}} & if\ \ i=SN \end{cases} \tag{17}$$

$$\left.\frac{\partial N_i^p}{\partial t}\right|_{sg} = \begin{cases} -\dfrac{I_{g,i}}{m_{i+1}-m_i}\eta_{p,i} & if\ \ i=1 \\ \dfrac{I_{g,i-1}}{m_i-m_{i-1}}\eta_{p,i-1} - \dfrac{I_{g,i}}{m_{i+1}-m_i}\eta_{p,i} & if\ \ i=2,\ldots,\ SN-1 \\ \dfrac{I_{g,i-1}}{m_i-m_{i-1}}\eta_{p,i-1} & if\ \ i=SN \end{cases} \tag{18}$$

where $I_{g,i}$ is the total surface growth rates due to PAH condensation and HACA for the i_{th} section and is always positive.

In the same manner, the source terms due to surface oxidation are obtained using the three-point method [82]. These source terms for aggregates and primary particles in the i_{th} section are as follows:

$$\left.\frac{\partial N_i^a}{\partial t}\right|_{ox} = \begin{cases} -\dfrac{I_{ox,i+1}}{m_{i+1}-m_i} + \dfrac{I_{ox,i}}{m_i} & if\ \ i=1 \\ \dfrac{I_{ox,i}}{m_i-m_{i-1}} - \dfrac{I_{ox,i+1}}{m_{i+1}-m_i} & if\ \ i=2,\ldots,\ SN-1 \\ \dfrac{I_{ox,i}}{m_i-m_{i-1}} & if\ \ i=SN \end{cases} \tag{19}$$

$$\left.\frac{\partial N_i^p}{\partial t}\right|_{ox} = \begin{cases} -\dfrac{I_{ox,i}}{m_{i+1}-m_i}\eta_{p,i+1} + \dfrac{I_{ox,i}}{m_i}\eta_{p,i} & if\ \ i=1 \\ \dfrac{I_{ox,i}}{m_i-m_{i-1}}\eta_{p,i} - \dfrac{I_{ox,i+1}}{m_{i+1}-m_i}\eta_{p,i+1} & if\ \ i=2,\ldots,\ SN-1 \\ \dfrac{I_{ox,i}}{m_i-m_{i-1}}\eta_{p,i} & if\ \ i=SN \end{cases} \quad (20)$$

where $I_{ox,i}$ is the oxidation rate for the i_{th} section in units of g/cc/sec and is always negative.

3.6 Fragmentation

While soot primary particles can reduce their size due to surface oxidation, soot aggregates are broken down into smaller aggregates via oxidation-driven fragmentation. In the present study, the fragmentation pattern is 1:1 which means each soot aggregate is broken down into two aggregates with an identical mass [78, 83]. Figure 3.1 represents a schematic of 1:1 fragmentation pattern, in which n_p is the number of primary particles per aggregate. All primary particles are assumed to have the same mass within an aggregate.

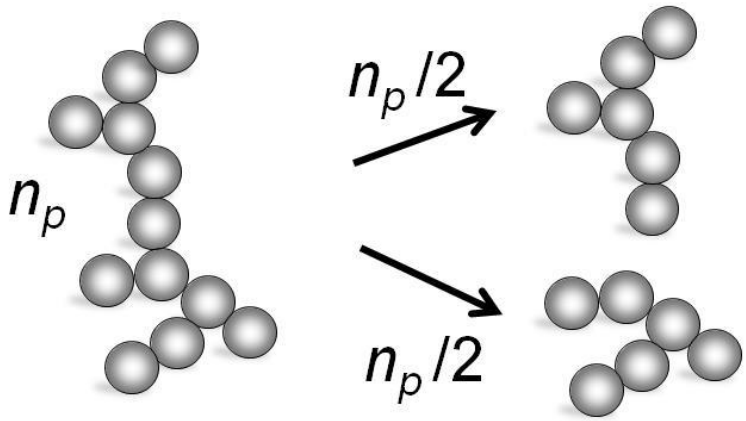

Figure 3.1: 1:1 fragmentation pattern (Reprinted from [78])

The fragmentation rate for aggregates in the i_{th} section is given by [84]:

$$S_i = A(n_{p,i})^{1/D_f} \tag{21}$$

where A is a coefficient that governs the overall fragmentation rate, which is taken to be a first order function of the soot oxidation rate and is calculated from:

$$A = Cr_{ox,s} \tag{22}$$

where $r_{ox,s}$ is the rate of soot mass removal due to oxidation per unit soot surface area and C is a constant and set to 1.0×10^5 [78, 83].

The source terms due to fragmentation for soot aggregates and primary particles are obtained as follows:

$$\left.\frac{\partial N_i^a}{\partial t}\right|_{fr} = \begin{cases} \Gamma_{i,i+1} S_{i+1} N_{i+1}^a & if\ \ i=1 \\ (\Gamma_{i,i}-1) S_i N_i^a - \Gamma_{i,i+1} S_{i+1} N_{i+1}^a & if\ \ i=2,\ldots,\ SN-1 \\ (\Gamma_{i,i}-1) S_i N_i^a & if\ \ i=SN \end{cases} \tag{23}$$

$$\left.\frac{\partial N_i^p}{\partial t}\right|_{fr} = \begin{cases} \dfrac{\Gamma_{i,i+1} S_{i+1} N_{i+1}^a n_{pah,i+1}}{fs} & if\ \ i=1 \\ (\Gamma_{i,i}-1) S_i N_i^a n_{pah,i} + \dfrac{\Gamma_{i,i+1} S_{i+1} N_{i+1}^a n_{p,i+1}}{f_s} & if\ \ i=2,\ldots,\ SN-1 \\ (\Gamma_{i,i}-1) S_i N_i^a n_{pah,i} & if\ \ i=SN \end{cases} \tag{24}$$

where $\Gamma_{i,i}$ and $\Gamma_{i,i+1}$ are breakage distribution functions and are calculated as below:

$$\Gamma_{i,i} = \frac{f_s - 2}{f_s - 1}$$
$$\Gamma_{i,i+1} = \frac{f_s}{f_s - 1}. \quad (25)$$

The breakage distribution functions are parameters to ensure the mass and number of aggregates as well as the size and number of primary particles are conserved by weighting the newly formed mass into two adjacent sections.

3.7 Summary

In this chapter, the soot sub-models incorporated in the present CFD model were described in detail. First, the chemical mechanism used in the present study were addressed. This chapter had been continued by explaining various soot sub-models including nucleation, coagulation, surface reactions, and concluded by fragmentation. In the next chapter, a temperature-history function for soot surface reactivity is tested on different high-pressure flames in order to investigate its validity at varying pressures.

Chapter 4 – Impact of Pressure-based HACA Rates on Soot Formation

4.1 Overview

There are several processes to occur in soot formation and destruction for which some in the growth regime require a better understanding. In this work, a consistent surface reactivity model, developed in recent years, has been implemented across various sooting laminar flames at varying pressures. The surface reactivity function proposed by Khosousi and Dworkin [12] is employed in the present study. It is based on the temperature history of soot particles. As the functionally dependent model has been derived and validated for atmospheric pressure flames, there are discrepancies between simulation and experiment that can be observed as pressures vary. One reason for these discrepancies could be explained by the fact that chemical reaction rates for the soot growth mechanism at atmospheric combustion do not adequately characterize the kinetics at higher pressures. Based on a recently published study [85], reaction rates for acetylene addition in the growth mechanism depend logarithmically on pressure and in the present study have been updated accordingly. It has been determined that after applying the new pressure-based acetylene addition reaction rate for the soot growth mechanism, the performance of the functionally dependent surface reactivity model improves in the wing regions of the flame. However, the quantity for soot concentration along the centerline of the flame is nearly independent of the surface reactivity model chosen and needs further investigation.

4.2 Introduction on Surface Growth

Although a large body of work on soot formation and oxidation has been conducted on atmospheric flames [12, 19, 21, 27, 67, 86, 87], many gaps still remain with regard to soot modelling at elevated pressures. Moreover, due to high-pressure industrial applications of combustion, studying higher pressure flames is at the center of attention for academics and industry professionals. There is a sufficient number of experimental studies on high pressure flames for different fuels including ethylene and ethane [10, 15, 17, 36, 88-101] with only a few numerical studies [22, 23, 102-104]. Although experimental studies are necessary for validation and also to assess soot formation and oxidation behaviour, numerical studies are faster and less expensive to generate results. Further, numerical analyses are needed to fully understand the causes of the behaviour seen in the experiments.

Soot surface reactivity, which represents the percentage of soot particle sites that are available for chemical reaction, has been the subject of various studies [8, 12, 21-23, 27, 72, 104, 105]. For modelling this reactivity, either a single constant value or a function which captures different flame properties has been used. For example, a fixed parameter, soot surface reactivity, α, of 0.078, was used in a previous work [21] in order to match the numerical results to the corresponding experimental data at atmospheric pressure. The concept of a temperature-history dependant α model has been tested in atmospheric combustion [12, 27], while at higher pressures, researchers have only used constant α values [22, 23, 102-104].

Eaves *et al.* [22, 23], Charest *et al.* [102, 103], and Liu *et al.* [104], numerically studied effects of different factors including pressure, conjugate heat transfer (CHT), gravity, and dilution on soot formation at higher pressures. Eaves *et al.* [22] conducted a sensitivity analysis on high

pressure laminar coflow diffusion ethane-air flames to perceive the effect of different parameters including soot surface reactivity, and pressure on maximum soot concentration along the centerline of the flame, and along the pathline passing through the maximum soot volume fraction, f_v. They used different constant α values of 0.0195, 0.039, 0.078, 0.156, and 0.332 for the calculations. In the aforementioned study, it is shown that soot concentration along the pathline of maximum soot is more surface-growth dominated than PAH-condensation dominated, while PAH condensation dominates the centreline of the flame. Also, as pressure is increased, the role of PAH condensation in surface growth becomes greater than that at lower pressures. These results led to later studies considering different constant α values and finding correlations between α and maximum f_v.

Contrary to [22, 104], Veshkini *et al.* [27] studied atmospheric pressure flames with a constant α for oxidation and with a functional α for formation which greatly improved the prediction of soot formation in those flames compared to a single constant α model. The function that Veshkini *et al.* proposed is based on temperature history, which depends on both temperature and residence time. Khosousi and Dworkin [12] applied the idea of temperature history to propose a novel functional α for both formation and oxidation rates. This model was tested for nine atmospheric pressure laminar coflow diffusion flames. Although the latter function was very successful in modelling different experimental data sets at atmospheric pressure, it has not yet been examined on higher pressures flames. To the current author's knowledge, this is the first research project assessing laminar coflow diffusion flames at varying pressures adopting a more predictive functional form for α.

In the present chapter, recent experimental data from Karataş and Gülder [15] has been studied numerically. The numerical solution obtained with the Khosousi and Dworkin function for α [12] is compared to the experimental results for pure ethylene flames at pressures of 1, 3, 5, and

7 atm and for nitrogen diluted ethylene flames at pressures of 5, 10, 15, and 20 atm. It should be mentioned that the goal of the present study was not to obtain a perfect match between numerical and experimental results, but rather a study of the physics of soot surface reactivity at higher pressure.

4.3 Soot Surface Reactivity

As mentioned in chapter 2, PAHs are soot precursors. The most accepted model to develop multi-ring aromatics is Hydrogen-Abstraction-Carbon-Addition (HACA) [6, 72] mechanism. HACA begins with the abstraction of an H atom by another H atom existing near the surface of the PAH molecule. It is followed by carbon addition, by acetylene, to form further aromatic rings. This is displayed in Fig. 4.1. Since soot particles are formed predominantly from aromatics, it is assumed that they have similar characteristics [8, 71, 72]. Thus, the chemical reaction sequences to build PAHs and soot are also presumed to be analogous. One of the major contributors to soot mass yield is surface growth of primary particles [8, 72]. Similar to PAH-HACA, soot particles grow via soot-HACA with the same reaction sequence.

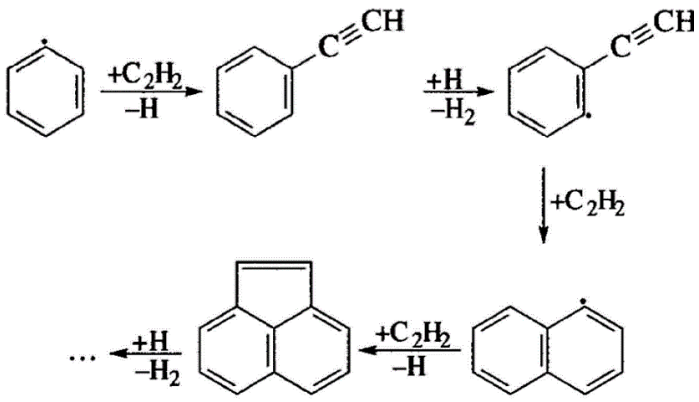

Figure 4.1: Formation of multi-ringed aromatics through HACA sequence (Reprinted from [106])

Since the probability of an available H atom on the surface of soot molecules to start the HACA mechanism is not 100%, not the entire soot surface area is available for chemical reaction. The portion of chemically active sites in soot particles which is named ‘soot surface reactivity’ is a significant parameter in soot formation and the numerical value of this factor is between 0 and 1, which 0 means there is no soot surface area is available, and 1 means the entire surface is accessible for chemical reaction. Soot surface reactivity, α, was first introduced by Frenklach and Wang [72] to account for surface structure and reconcile the inaccuracies in numerical studies.

Dworkin *et al.* [21] and Eaves *et al.* [22] showed that with a constant α, the present numerical model is able to predict reasonable results; however, for each flame and burner configuration it needs to be retuned with a different α value. Based on the literature [58, 72, 107], soot surface reactivity depends on the temperature to which a soot particle has been exposed. Similarly, experimental studies [107, 108] define residence time as a significant factor in determining α. In this sense, Veshkini *et al.* [27] proposed an α function, Eq. (1), which includes the concept of temperature history, or temperature aging:

$$\alpha = \frac{6974.6}{T_a^2} \exp\left(\frac{-88.06}{T_a}\right), \tag{1}$$

where T_a is thermal age and is defined as the integral of temperature with respect to residence time along a fluid parcel pathway, *S*, and is calculated as:

$$T_a = \int_S T dt\,. \tag{2}$$

Khosousi and Dworkin [12] proposed a variation on that form of α which captures correctly the peak soot concentrations and smoking character for nine flames and burner configurations all at atmospheric pressure. Equation (3) is the mathematical form of this model:

$$\alpha = (\frac{T_{a,\max}}{T_a})^{2.2} \exp\left[2.4(0.85 - \frac{T_{a,\max}}{T_a}) \right], \quad (3)$$

where the $T_{a,\max}$ is the value for the thermal age at the location of maximum soot volume fraction.

Figure 4.2 displays contours of α of the Khosousi and Dworkin soot surface reactivity model [12] for the pure ethylene flames at varying pressures. This figure shows two important points; first, as pressure increases, the profile for α seems to be pressed towards the centerline of the flame as well as towards the nozzle of the flow field. Second, as pressure increases, α reaches its maximum at a lower height-above-the-burner (HAB) along the off-centerline areas of the flame. This may be due to the increase of T_a at lower HABs with increasing pressure. The contours of the present α model [12] for the nitrogen diluted ethylene flames at varying pressures follow the same trend as well.

Unlike the Veshkini *et al.* model [27], the Khosousi and Dworkin equation [12] is capable of predicting both formation and oxidation adequately although it has not been examined for high-pressure flames. The other difference between these two models is the parameter $T_{a,\max}$, which changes as the location of peak f_v varies. This functionality adjusts α for each flame without changing the soot surface reactivity model. Figure 4.3 displays the impact of T_a on α for pure ethylene flames at varying pressures at two different locations on the centerline and the wing of

the flame. It shows that α reaches approximately the same peak value at all pressures, then declines along both locations of the wing region and the centerline of the flames. Also, as pressure increases, α reaches this value at higher values of T_a. Again, repeating Fig. 4.3 for the nitrogen diluted ethylene flames result in the same trend as pressure increases.

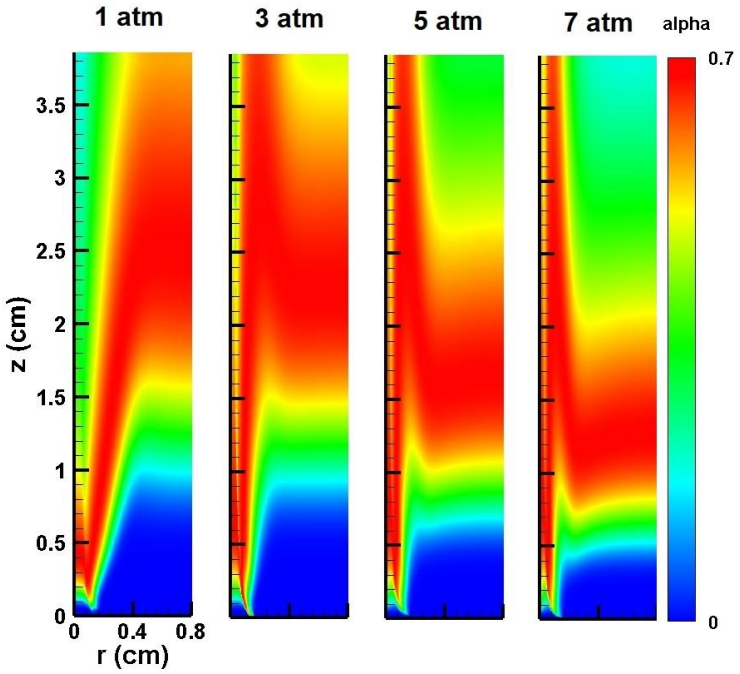

Figure 4.2: Soot surface reactivity, α function [12] contours of pure ethylene flames at different pressures of 1, 3, 5, and 7 atm

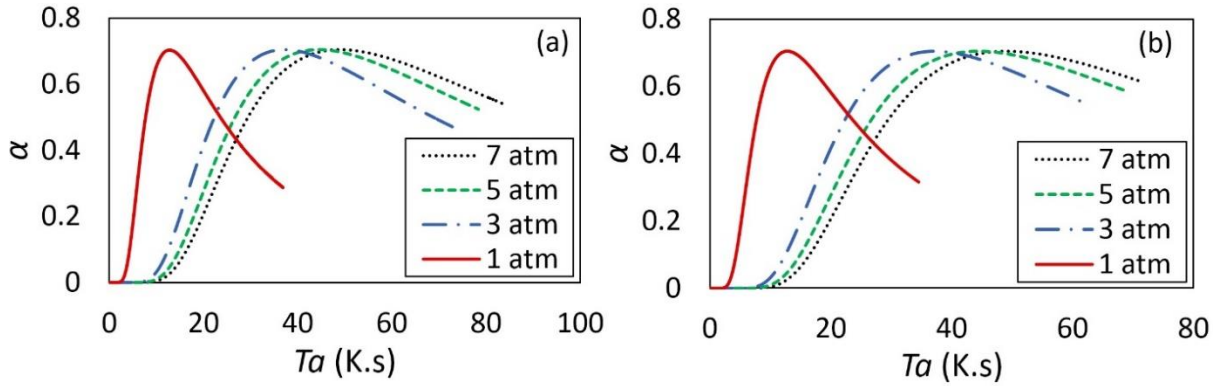

Figure 4.3: Comparison of the functional form of α [12] versus the temperature-history, a) along the pathline of maximum f_v, and b) along the centerline of the flame for pure ethylene flames at different pressures of 1, 3, 5, and 7 atm

The present study proceeds by examining the functional form of α proposed by Khosousi and Dworkin [12] for both formation and oxidation processes, then investigates advantages and drawbacks leading towards a more improved model. The temperature-history dependant α function does not lead to a significant increase in computational cost as it only needs to be evaluated every thousand or so time steps for steady systems.

The other important aspect that should be noted is, in most chemical kinetic mechanisms, reaction rates for HACA growth have been based on reaction rates at atmospheric pressure. Based on [27], the reaction rate for an individual reaction of C_2H_2 addition in the HACA-based soot surface growth and oxidation mechanism is as follows:

$$R = \alpha\, k\, [C_2H_2][C_{soot}\circ], \tag{4}$$

where R is the reaction rate, α is the surface reactivity, k is the global rate coefficient, and $[C_2H_2]$ and $[C_{soot}\circ]$ are concentrations of acetylene and dehydrogenated sites. Since the reaction rates for HACA growth are those suitable for atmospheric pressure, they may not adequately characterize HACA growth at varying pressures. A recent study by Frenklach *et al.* [85] indicates that HACA growth reaction rates for acetylene addition depend logarithmically on pressure. Based off of this study, a new model for the reaction rates for soot HACA growth is introduced and Eq. (4) is updated for higher pressure combustion as follows:

$$R = (1 + \log(p))\, \alpha\, k\, [C_2H_2][C_{soot}\circ]. \tag{5}$$

where p is the operating pressure. At 1 atm, Eq. (4) and Eq. (5) are identical and both predict the same reaction rate in an individual reaction of C_2H_2 addition in the HACA-based soot surface growth and oxidation mechanism. Hereinafter, the model with the atmospheric HACA growth rates and the temperature-history dependant α [12] is referred to as "Khosousi and Dworkin model" and the model with the pressure-based reaction rate of acetylene addition in the HACA mechanism and temperature-history dependant α is referred to as the "present model". These models are summarized in Table 4.1.

Tabel 4.1: Comparison of Khosousi and Dworkin model [12] and the present model

Name	**Soot HACA model**	**α model**
Khosousi and Dworkin	Atmospheric HACA growth rates $R = \alpha k [C_2H_2][C_{soot}\circ]$	$\alpha = (\frac{T_{a,\max}}{T_a})^{2.2} \exp\left[2.4(0.85 - \frac{T_{a,\max}}{T_a})\right]$
Present model	Pressure-based HACA growth rates $R = (1 + \log(p))\, \alpha k [C_2H_2][C_{soot}\circ]$	$\alpha = (\frac{T_{a,\max}}{T_a})^{2.2} \exp\left[2.4(0.85 - \frac{T_{a,\max}}{T_a})\right]$

4.4 Flame and Model Description

4.4.1 Burner Configuration

A brief description of the burner configuration that is modelled in the present work is given here; however, the details of the apparatus used for the experimental study can be found in [15, 36]. A co-annular coflow laminar diffusion burner working at varying pressures has been studied. The inner diameter at the burner rim is 3 mm. The thickness of the fuel tube decreases gradually from the rim to the edge of the fuel tube to prevent the formation of recirculation zones. The flames simulated in this chapter are the same as the flames in the experiment [15], including the pure

ethylene flames at pressures of 1, 3, 5, and 7 atm and N_2 diluted ethylene flames at pressures of 5, 10, 15 and 20 atm. For the pure ethylene flames, the mass flow rates of ethylene and air are kept at 0.48 mg/s, and 340 mg/s respectively at all pressure levels. For the diluted flames, the mass flow rates of N_2, ethylene, and air are kept at 0.96 mg/s, 0.48 mg/s, and 340 mg/s respectively at all pressure levels.

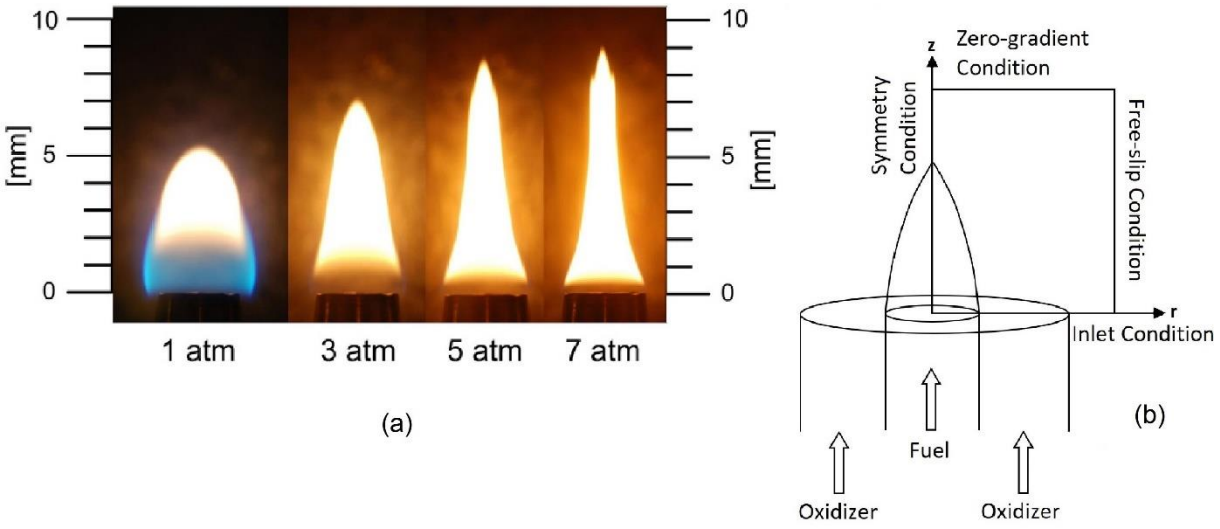

Figure 4.4: Flame and burner configuration, a) A still photo of the laminar co-annular ethylene-air flame at pressures up to 7 atm (Reprinted from [15]), b) Schematic representation of the burner and flame, including coordinate axes and computational domain boundaries. (Image is not drawn to scale)

Figure 4.4 displays the ethylene-air flame pictures and the schematic representation of the burner and the boundary conditions. Considering Fig. 4.4, to further explain the choice of inlet boundary condition, one option is to move the bottom boundary of the computational domain down below the fuel tube exit. This would necessitate the modelling of the solid tube material as either adiabatic, or thermally participating. The term conjugate heat transfer (CHT) is used to describe processes which involve the combination of heat transfer between solids and fluids. An anchored flame will heat the fuel tube, leading to CHT, although permitting CHT in the model does not

necessarily mean that it would occur. Although CHT has been utilized with the CoFlame code in the past [23] with great additional computational cost, it is not considered in the current study. Also in consultation with the authors of the experimental paper [15], it was noted that full characterization of liftedness and heat conduction back down toward the burner was not conducted. Therefore, CHT is not conducted in the present work.

4.4.2 Numerical Model

The fully coupled governing equations for mass, momentum, energy, and species mass fraction are solved using the CoFlame code [14]. The details of gaseous phase governing equations and boundary conditions can be found in chapter 2. The computational domain is formed as a non-uniform axisymmetric grid, with 150 control volumes in the radial direction (r) and 400 control volumes in the axial direction (z), with the resolution of dr = 0.013 mm and dz = 0.016 mm in the flame region.

A fixed soot sectional model is used, in which the soot particle mass is divided into thirty-five sections logarithmically. The soot particle dynamics model consists of inception, Hydrogen Abstraction Carbon Addition (HACA), Polycyclic Aromatic Hydrocarbon (PAH) condensation, coagulation, and fragmentation. The soot sectional model solves two equations per section to obtain number densities of aggregates and primary particles. The chemical mechanism used in the present work is a modified version of an earlier mechanism presented in [21, 109], which is described in detail in [18]. Further details can be found in chapter 2 and chapter 3.

4.5 Results and Discussion

4.5.1 Pure Ethylene Flames

A comparison between the simulation results and the experimental data [15] for pure ethylene flames is made for the maximum soot volume fraction at pressures from 1 to 7 atm, which is shown in Fig. 4.5. The uncertainty in soot volume fraction for the experimental data is taken as 40% [15], which is comparable to other experimental studies at elevated pressures. Figure 4.5 shows some important aspects; first, the model with a constant α value of 0.5 follows closely the trend of the experimental values; however, it only predicts the peak f_v of the experimental data within the uncertainty for a pressure of 3 atm. Second, although Khosousi and Dworkin model [12] leads to a prediction of higher peak f_v compared to the constant α model, it is again only able to predict the peak f_v of the experimental data within the uncertainty at 3 atm. Third, both the model with an constant α value of 0.5 and Khosousi and Dworkin model [12] predict the experimental results for the other three pressures in the same order of magnitude. Forth, the present model predicts the peak f_v of the experimental data within the uncertainty at all pressures of 1, 3, 5, and 7 atm. The ratios of the numerical result from Khosousi and Dworkin model [12] and the present model to the experiment for maximum soot volume fraction are 0.54 and 1.15 at 1 atm, 0.78 and 1.15 at 3 atm, 0.48 and 1.01 at 5 atm, and 0.35 and 0.69 at 7 atm respectively.

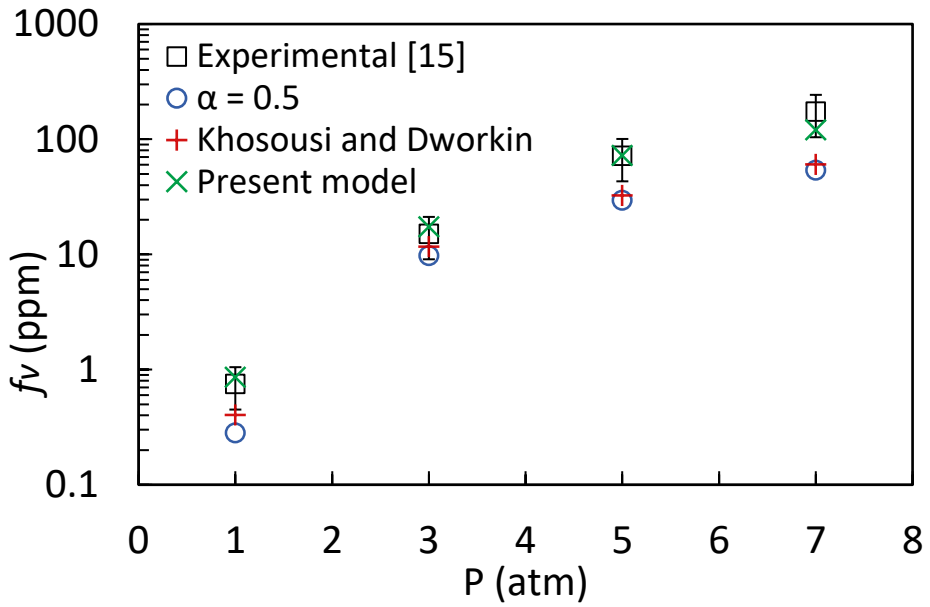

Figure 4.5: Comparison of global maximum soot volume fraction in the numerical study for constant α value of 0.5, Khosousi and Dworkin model [12], and the present model, with the experimental study [15].

A comparison between the experimental and the numerical results for the peak values of soot volume fractions are summarized in Table 4.2. The numbers in the brackets in the experimental column are lower and upper bounds of the experimental data range. Table 4.2 shows that only the present model is capable of predicting the maximum soot concentration within the experimental uncertainty for all pressures from 1 to 7 atm.

Table 4.2: Comparison of peak soot volume fraction values (ppm) between experimental and numerical results for the pure ethylene flames.

Flames	**Exp. [15]**	**α = 0.5**	**Khosousi and Dworkin [12]**	**Present model**
1 atm	[0.45, 1.05]	0.28	0.40	0.86
3 atm	[9, 21]	9.8	11.7	17.4
5 atm	[43, 101]	29.5	32.4	72.2
7 atm	[104, 243]	54.1	60.3	120.4

An assessment of the overall shape of the flame is necessary to ensure that simulations predict the physical characteristics of the flame such as flame length. Flame length, which is

defined by the axial location where the percent stoichiometric air is 100%, is inversely proportional to flame temperature [110]. For this reason, flame temperature is an indicator of flame length, and Fig. 4.6 displays a comparison of temperature contours for the experiment and the present model.

Based on the temperature field which is displayed in Fig. 4.6, pressure has a significant impact on the temperature map. When considering the overall flame shape, the simulation reproduces what is seen in the experiment with acceptable accuracy. As pressure increases, the flame becomes thinner and the flame length increases, and the location of the peak temperature changes from the inner part of the flame to the wings. The maximum values for the temperature obtained from the present model are 2077, 2041, 1978, and 1998 K at 1, 3, 5, and 7 atm, respectively. The maximum values for the temperature obtained from the experiment [15] are 2080, 2021, 1949, and 1963 K at 1, 3, 5, and 7 atm, respectively. It should also be noted that the experimental temperature map does not have smooth edges which is due to a large drop from the flame temperature to the coflow air temperature. This comparison indicates that the simulation can capture the trend for temperature. For all pressure levels except 1 atm, the simulated flame lengths are slightly smaller than the experimental ones, which can contribute to a different soot formation field than the experimental ones. Despite these differences, the simulation captures the correct maximum temperature and trend for the temperature field compared to the experimental result.

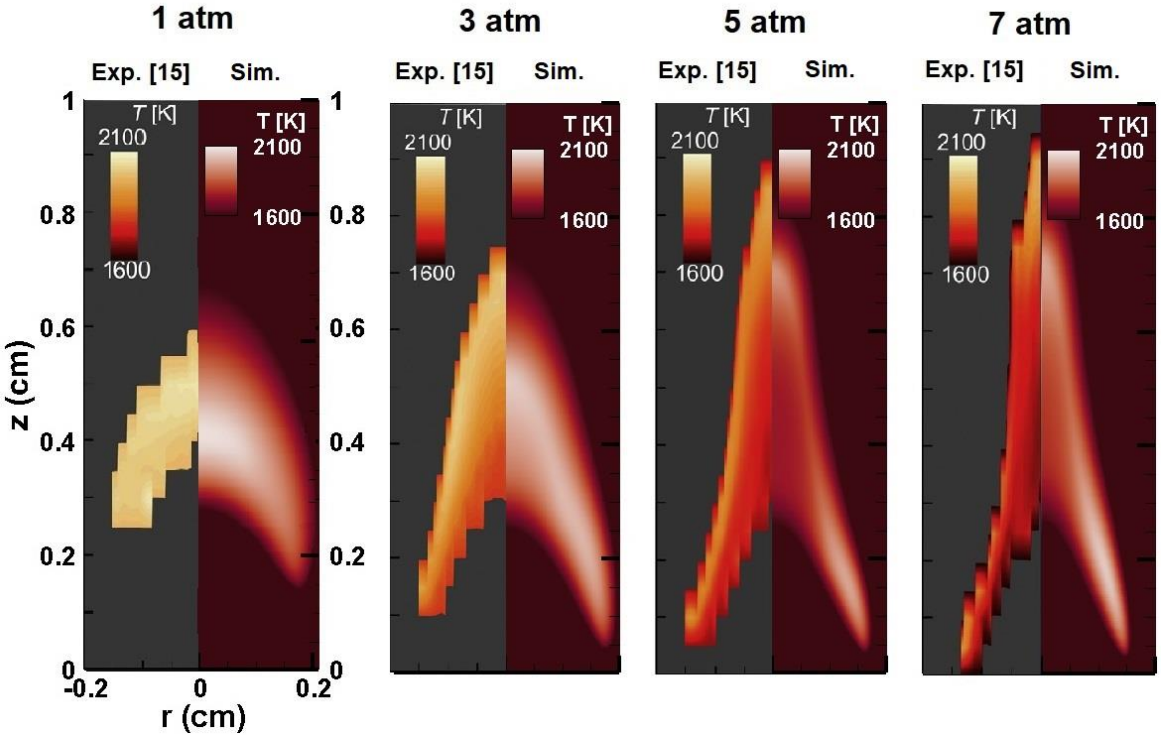

Figure 4.6: Comparison of temperature contours of the pure ethylene flames for the experimental study [15] and the present model at different pressures of 1, 3, 5, and 7 atm

Furthermore, Fig. 4.7 displays a comparison of the soot yield percent versus the height-above-the-burner (HAB) between the experimental and the simulation results brings more detailed information about the impact of utilizing various soot surface reactivity models.

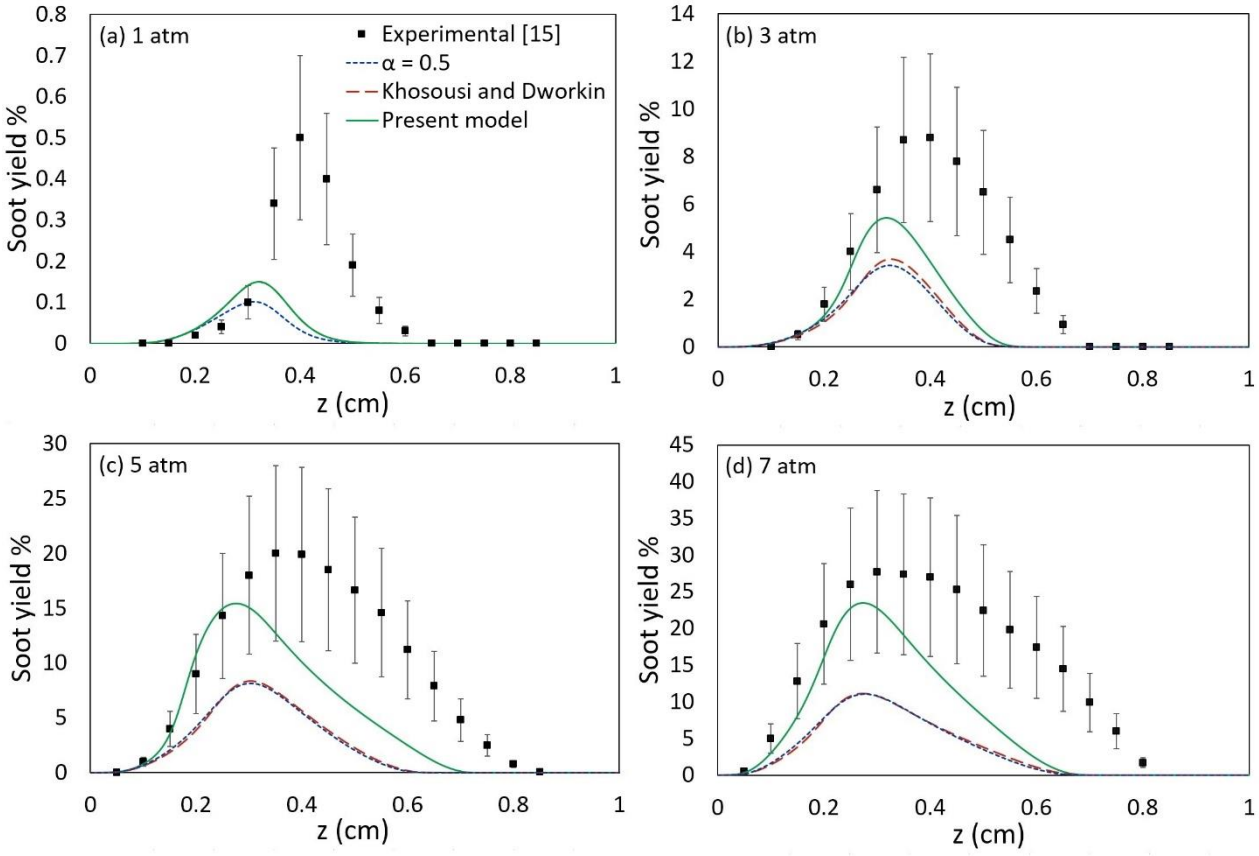

Figure 4.7: Comparison of soot yield percent as a function of the height-above-the-burner (HAB) (z), for the experimental study [15], and simulations applying a constant α value of 0.5, Khosousi and Dworkin model [12], and the present model for pure ethylene flames at different pressures a) 1 atm, b) 3 atm, c) 5 atm, and d) 7 atm.

Figure 4.7 shows some important points; first, since at 1 atm, there is no difference between Khosousi and Dworkin model [12] and the present model, and the results of simulation utilizing both models are exactly the same. Second, as pressure increases, the prediction of the soot yield percent for the model with a constant α value of 0.5 and Khosousi and Dworkin model [12] starts to cluster together and to deviate from the results utilizing the present model. Third, the present model leads to a better prediction of the soot yield percent among the three soot surface reactivity models. Fourth, as pressure increases, the effectiveness of the present model in predicting the soot yield percent becomes more significant. Lastly, the present model leads to a more accurate

prediction in the formation region compared to the oxidation region. Formation region is simply defined by the region of the flame in which soot particles grow and their masses increase, whereas in oxidation region, soot particles and aggregates reduce in size.

In the experimental study [15], the maximum soot volume fraction at 1 and 3 atm lays along the centerline of the flame which is not captured with the numerical model. Therefore, a comparison of f_v along the centerline between the experimental study [15] and the simulations utilizing a constant α value of 0.5, Khosousi and Dworkin model [12], and the present model, which is displayed in Fig. 4.8, provides insight into the discrepancy.

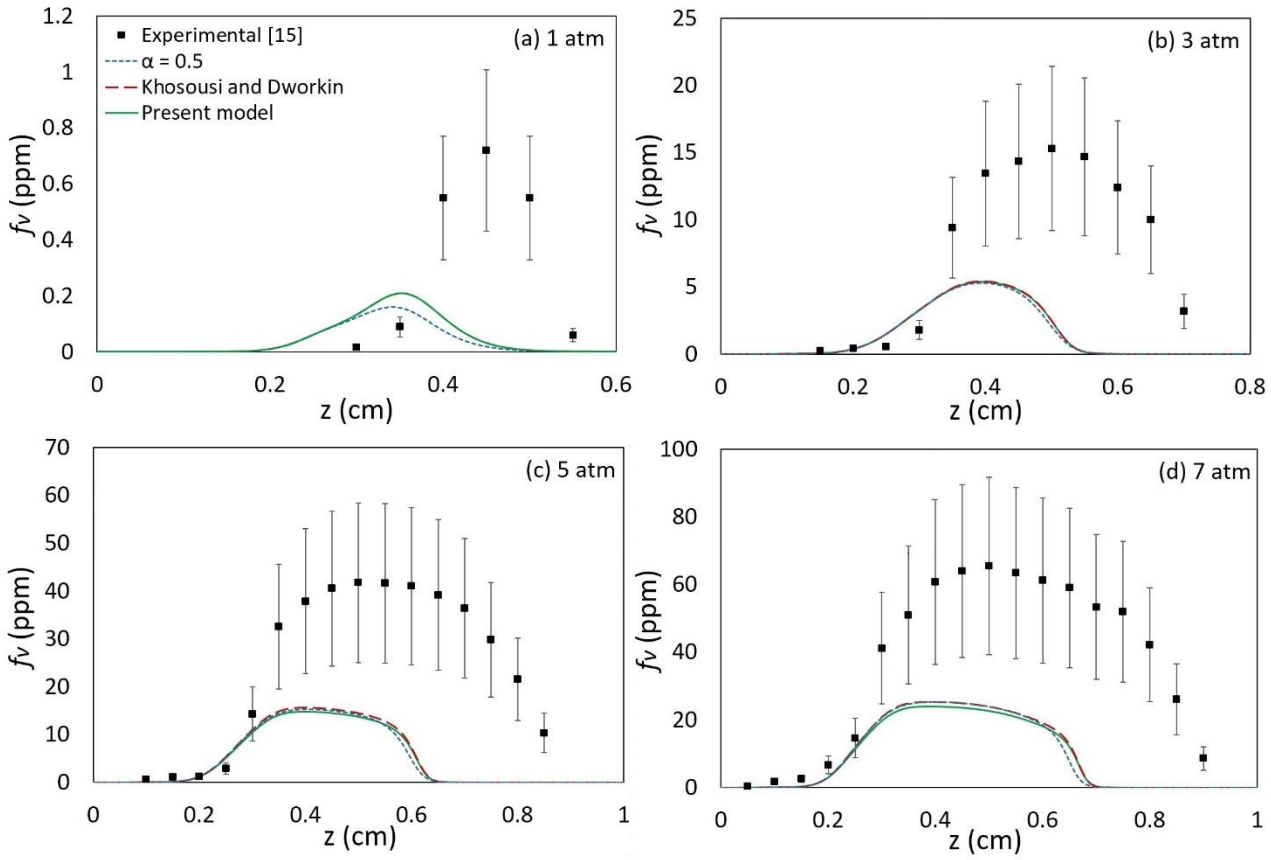

Figure 4.8: Comparison of f_v versus the height-above-the-burner (HAB) (z), along the centreline of the flame for the experimental study [15], and simulations applying a constant α value of 0.5, Khosousi and Dworkin model [12], and the present model for pure ethylene flames at different pressures a) 1 atm, b) 3 atm, c) 5 atm, and d) 7 atm.

As can be observed in Fig. 4.8, as pressure increases, all models underpredict the location of peak soot concentration on the centerline. It also shows that despite underpredicting f_v, all models lead to the prediction of soot concentration along the centerline of the flames within the correct order of magnitude at all pressures. It is noteworthy that due to the cumbersome practical accessibility to trace the pathline of peak f_v, experimental data for soot concentration along that pathline is not available for comparison purposes with the simulation results.

Comparing Fig. 4.7 and Fig. 4.8 shows that the most important difference between the results of the three soot surface reactivity models is at the wing region, where the present model shows a greater increase in f_v compared to the other two models. However, along the centerline of the flames, the present model leads to a decrease in f_v as pressure increases, albeit a negligible one, due to the domination of PAH condensation and not HACA, which is consistent with the results of the study of Eaves *et al.* [22]. The numerical results utilizing the present model predict the peak f_v at the wings at all pressures, which is in contrast with the experiment of the 1 and 3 atm pure ethylene flames [15]. The experiment shows that the peak value for these flames lays at the centerline of the flames.

4.2 N_2 Diluted Ethylene Flames

The effect of soot surface reactivity is also analyzed for cases of N_2 diluted ethylene flames at a pressure range of 5, 10, 15, and 20 atm. Overall features are similar to the pure ethylene flames presented in the previous section. A comparison between the simulation results and the experimental data [15] for N_2 diluted ethylene flames is made for the maximum soot volume fraction at pressures from 5 to 20 atm, which is shown in Fig. 4.9. Again, the uncertainty in soot volume fraction for the experimental data is taken as 40% [15].

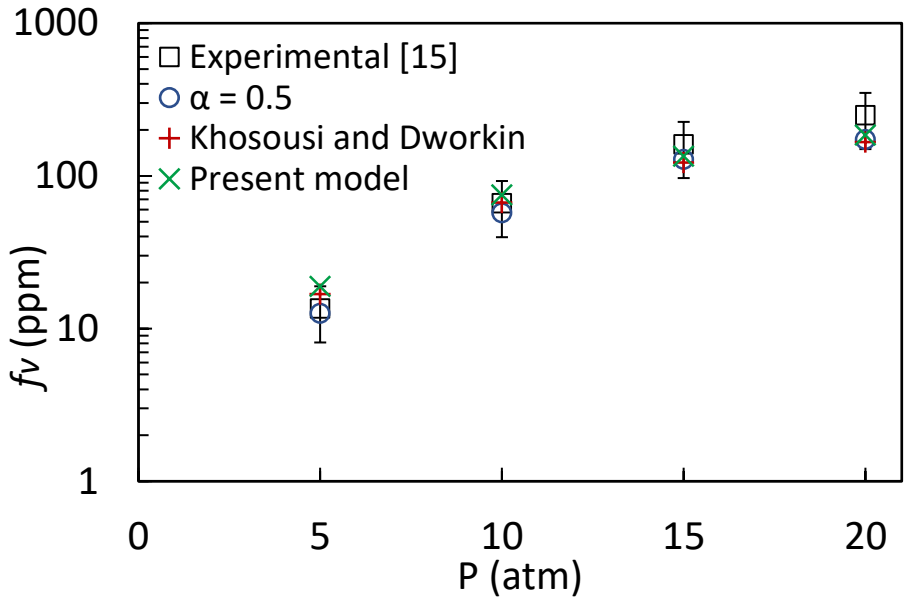

Figure 4.9: Comparison of global maximum soot volume fraction in the numerical study for a constant α value of 0.5, Khosousi and Dworkin model [12], and the present model, with the experimental study [15] for N_2 diluted ethylene flames at different pressures of 5, 10, 15, and 15 atm.

Figure 4.9 shows some important aspects; first, all soot surface reactivity models are able to predict the peak f_v of the experimental data within the experimental uncertainty at all pressures. Second, as pressure increases, the prediction of peak f_v for all the three α models lumps together; however, the present model predicts a higher peak f_v compared to the other two soot surface reactivity models at all pressures, which is similar to the results of the pure ethylene flames. The ratios of the numerical result utilizing Khosousi and Dworkin model [12] and the present model to the experiment for maximum soot volume fraction is 1.24 and 1.45 at 5 atm, 1.01 and 1.14 at 10 atm, 0.76 and 0.84 at 15 atm, and 0.67 and 0.74 at 20 atm respectively. The peak values of soot volume fractions and the comparison between the experimental and the numerical results are summarized in Table 4.3. Numbers in the brackets in the experimental column are lower and upper bounds of the experimental data range.

Table 4.3: Comparison of peak soot volume fraction values (ppm) between experimental and numerical results for the N_2 diluted ethylene flames.

Flames	**Exp. [15]**	**α = 0.5**	**Khosousi and Dworkin [12]**	**Present model**
5 atm	[8, 19]	12.6	16.8	18.9
10 atm	[39, 91]	57.1	66.8	75.1
15 atm	[96, 225]	128.5	122.3	134.5
20 atm	[150, 349]	173.1	166.6	184.9

The temperature fields for N_2 diluted ethylene flames are displayed in Fig. 4.10 in order to check the overall shape of the flames. The present model reproduces the overall shape of the flames seen in the experiment with acceptable accuracy. As pressure increases, the flame becomes thinner and the flame length increases, and the location of the peak temperature shifts from the inner part of the flame to the wings. The maximum values for the temperature obtained from the simulation applying the present model are 1988, 1959, 1951, and 1946 K at 5, 10, 15, and 20 atm, respectively. The maximum values for the temperature obtained from the experiment [15] are 2022, 1982, 1955, and 1948 K at 5, 10, 15, and 20 atm, respectively. Similar to the pure ethylene flames, this comparison indicates that the simulation can capture the trend for temperature. For all simulations, the flame lengths are slightly smaller than the experimental ones, which can contribute to a different soot formation field than the experimental ones. Despite that, the simulation captures the correct maximum temperature and trend for the temperature field compared to the experimental result.

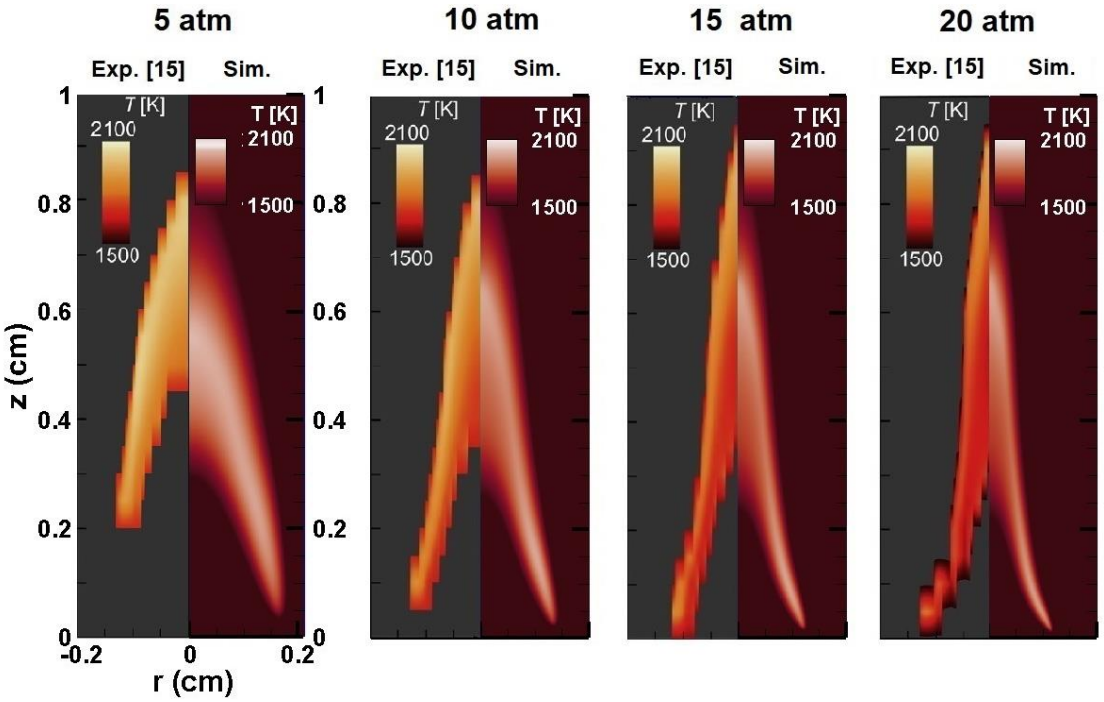

Figure 4.10: Comparison of temperature contours of the N_2 diluted ethylene flames for the experiment [15] and simulations applying the present model at different pressures of 5, 10, 15, and 20 atm.

A comparison of the soot yield percent versus HAB between the experimental and the simulation results reveals more detailed information about the impact of utilizing various α models on the nitrogen diluted ethylene flames. This comparison which is displayed in Fig. 4.11, shows some important points; first, all models lead to a more accurate prediction in the formation region than in the oxidation section. Second, as pressure increases, the prediction of the soot yield percent for the model with a constant α value of 0.5 and Khosousi and Dworkin model [12] starts to cluster together and to deviate from the results of the simulation utilizing the present model. Lastly, although all models underpredict the location of peak soot yield percent compared to the experimental result, the present model leads to a better prediction of the maximum soot yield percent at all pressures. This underprediction of the location of peak soot yield percent may be due to the smaller flame length in the simulations and underprediction on the centerline of the flames.

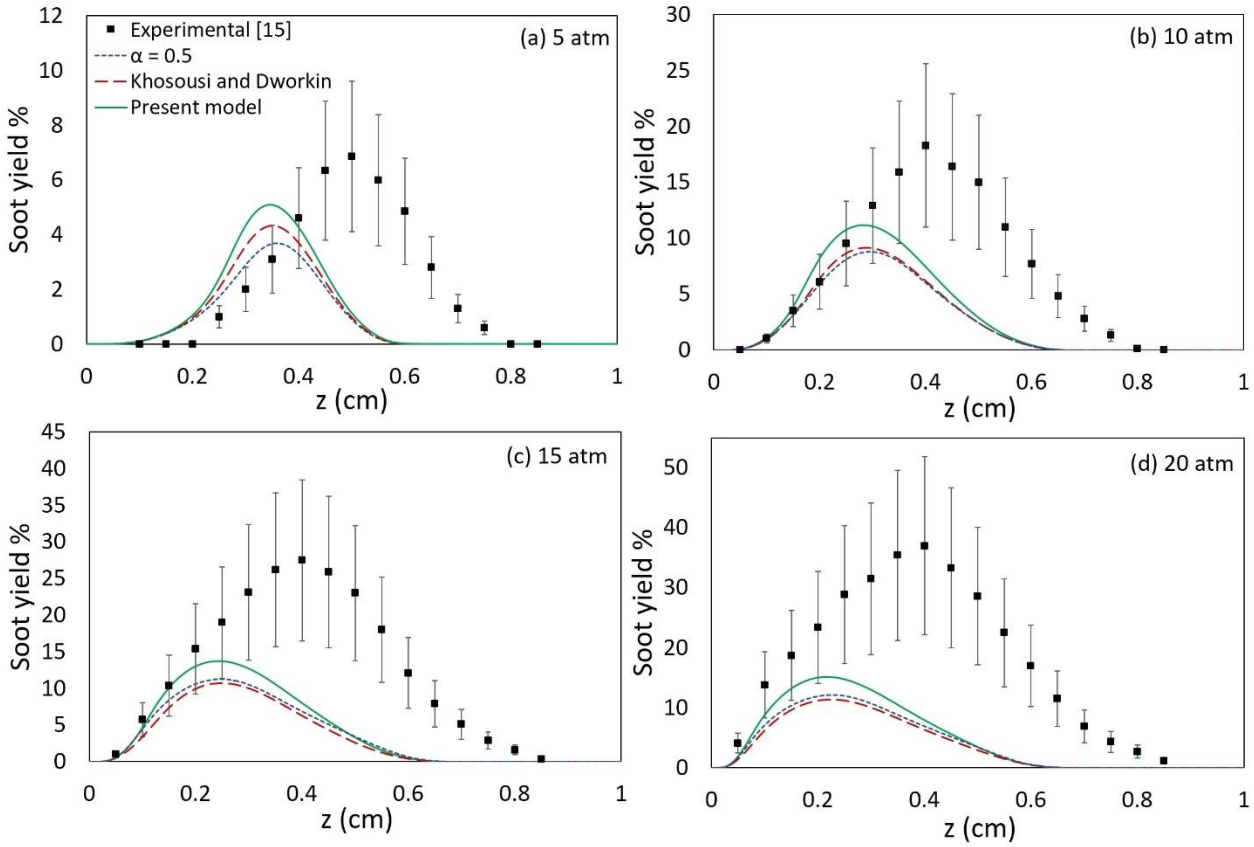

Figure 4.11: Comparison of soot yield percent as a function of the height-above-the-burner (HAB) (z), for the experimental study [15] and simulations applying a constant α value of 0.5, Khosousi and Dworkin model [12], and the present model for N_2 diluted ethylene flames at different pressures a) 5 atm, b) 10 atm, c) 15 atm, and d) 20 atm.

Once again, for a more thorough investigation of the impact of these three models on soot formation and oxidation, a comparison of f_v as a function of HAB along the centerline between the experimental study [15] and the simulations implementing a constant α value of 0.5, Khosousi and Dworkin model [12], and the present model for N_2 diluted ethylene flames at different pressures from 5 to 20 atm is required. This comparison is displayed in Fig. 4.12.

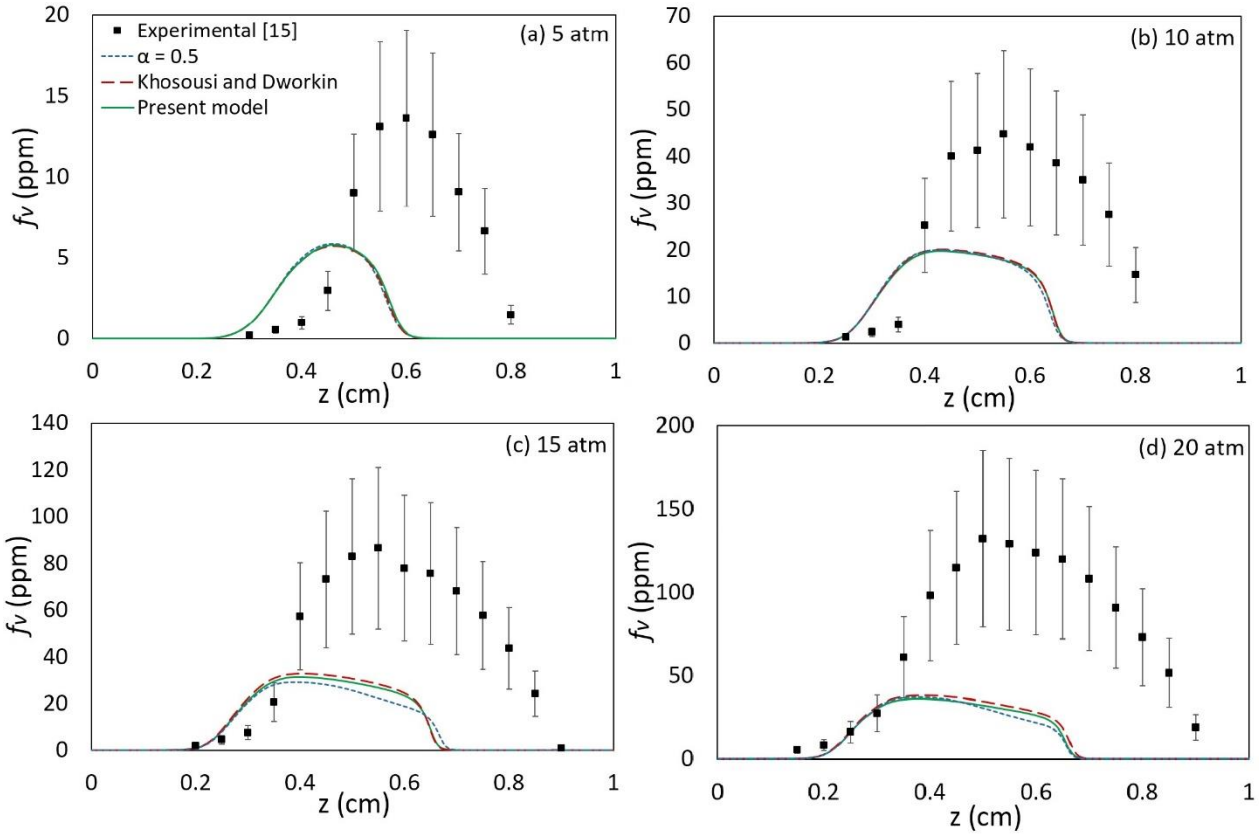

Figure 4.12: Comparison of f_v versus the height-above-the-burner (HAB) (z), along the centerline of the flame for the experimental study [15], and simulations applying a constant α value of 0.5, Khosousi and Dworkin model [12], and the present model for the N_2 diluted ethylene flames at different pressures a) 5 atm, b) 10 atm, c) 15 atm, and d) 20 atm.

As can be observed in Fig. 4.12, as pressure increases, all models capture the location of peak soot concentration on the centerline more precisely. It also shows that despite underpredicting f_v, all models lead to the prediction of soot concentration along the centerline of the flames within the same order of magnitude at all pressures. Although all three surface reactivity models underpredict the quantity and the location of peak soot concentration, they capture the correct trend of soot formation and decomposition as the pressure increases. At 5 atm, all three models predict a very similar profile for f_v with respect to HAB. As pressure increases the results of these three models deviate from each other in a way that Khosousi and Dworkin model [12] predicts the

highest f_v, then the present model and the constant α model consecutively. It again should be noted that due to the cumbersome practical accessibility to trace the pathline of peak f_v, experimental data for soot concentration along that pathline is not available for comparison purposes with the simulation results.

4.6 Summary

The effect of surface reactivity of soot particles in pure ethylene flames at pressures of 1, 3, 5, and 7 atm and N_2 diluted ethylene flames at pressures of 5, 10, 15, and 20 atm was studied. A new pressure-based reaction rate of acetylene addition in the HACA mechanism were introduced and were evaluated for their use in varying pressure flames. The employed soot surface reactivity model in the present study is the same as in the study conducted by Khosousi and Dworkin [12]. The same surface reactivity model is implemented for both formation and oxidation processes, but its impact on oxidation in these flames is negligible which is the same as that on the atmospheric flames in a previous study [12]. For pure ethylene flames, Khosousi and Dworkin model [12] is capturing qualitative trends, while the distribution and quantities still remain the subject of further inquiry. The present model is able to predict the peak f_v within the experimental uncertainty at all pressures; however, this model could not capture the peak f_v along the centerline of the 1 atm pure ethylene flame correctly. Since none of the models could capture the maximum soot concentration along the centerline of the 1 atm flame, this inconsistency highlights the need to better understand the physical processes that are occurring in the central/pyrolysis region of that flame. As pressure increases the effectiveness of the present model in predicting the soot yield percent becomes more significant. For the N_2 diluted ethylene flames, all of the three models capture the peak f_v within the experimental uncertainty; however, the present model leads to a prediction of higher values

compared to the other two models. Moreover, altering the soot surface reactivity models does not lead to any significant differences in prediction of f_v along the centerline of the flame for both pure and nitrogen diluted ethylene flames. One area of current and future inquiry relates back to the model for inception, and the potential participation of PAHs with aliphatic chains, which may work to change the distribution of soot within the flame.

Chapter 5 – Influence of Pressure on Near Nozzle Flow Field on Soot Formation

Corresponding Publication: A. Mansouri, N.A. Eaves, M.J. Thomson, S.B. Dworkin, Influence of pressure on near nozzle flow field and soot formation in laminar co-flow diffusion flames, Combustion Theory and Modelling 23 (2019) 536-548.

The roles of each author of this corresponding publication were addressed in detail in section 1.4.

5.1 Overview

While most fundamental studies have utilized the coflow laminar diffusion flame configuration to study the effect of pressure on soot, there is a lack of investigations into the effect of pressure on the flow field of diffusion flames and the resultant influence on soot formation. A recent work [111] has displayed that recirculation zones can form along the centreline of atmospheric pressure diffusion flames. This chapter seeks to investigate whether these zones can form due to higher pressure as well, which has never been explored experimentally or numerically.

The CoFlame code, which models coflow laminar, sooting, diffusion flames, is validated for the prediction of recirculation zones using experimental flow field data for a set of atmospheric pressure flames. The code is subsequently utilized to model ethane-air diffusion flames from 2 to 33 atm. Above 10 atm, recirculation zones are predicted to form. The reason for the formation of the zones is determined to be due to increasing shear between the air and fuel steams, with the air stream having higher velocities in the vicinity of the fuel tube tip than the fuel stream. This increase in shear is shown to be the cause of the recirculation zones formed in previously investigated atmospheric flames as well. Finally, the recirculation zone is determined as a probable cause of

the experimentally observed formation of a large mass of soot covering the entire fuel tube exit for an ethane diffusion flame at 36.5 atm. Previously, no adequate explanation for the formation of the large mass of soot existed.

5.2 Introduction

There have been a number of recent experimental investigations on the effect of pressure on soot formation in a laminar coflow flame configuration [10, 11, 15, 17, 36, 91-93, 95-97, 104, 112-116]. This configuration is utilized due to the simplified geometry, yet still allowing for investigation of the possible effects of diffusion and mixing. These studies concluded that maximum soot volume fraction increased with increasing pressure; however, the study by Joo and Gülder [11] had the interesting result of soot volume fraction reaching a peak at 55 atm, then monotonically declining as pressure was raised further. A brief communication by Mandatori and Gülder [13] demonstrated another unique phenomenon where at 36.5 atm the entire ethane fuel stream converted to soot.

To compliment these experimental investigations, multiple numerical studies have been performed to attempt to understand the reasons for the experimentally observed influence of pressure on soot formation. Most studies relied on simplified soot models that had limited ability to provide insights into how the mechanisms of soot formation are influenced [102, 103, 116-120]; however, others have used the more advanced method of moments [96] or sectional soot formation models [22, 23, 104] that utilize PAH-based soot nucleation and condensation models. The CoFlame code [14], has been validated and extensively used to investigate soot formation under a wide range of conditions, including high pressure. These advanced studies concluded that the experimentally observed increase in soot formation with increasing pressure was due to the

positive feedback nature of soot formation, instigated by density increases. In addition, the study in [23] demonstrated the importance of extending the computational domain to model below the exit plane of the fuel tube and including a conjugate heat transfer (CHT) model within numerical simulations of high pressure sooting diffusion flames. However, there still has been no adequate explanation of the reason for the complete conversion of ethane at 36.5 atm observed in [13], even with the investigations of Eaves, Thomson, Dworkin, and co-workers on these flames [22, 23].

To date, there are limited studies on the effect of pressure on the flow field of coflow diffusion flames and the subsequent effect of the flow field on soot formation. In a recent work, Xiong *et al.* [111] experimentally and numerically displayed that recirculation zones can form near the nozzle of atmospheric pressure coflow laminar diffusion flames when the fuel density is greater than that of air. Additionally, they concluded that in order to numerically predict the recirculation zones, the computational domain should extend into the fuel tube, similar to the conclusions of [23]. Xiong *et al.* asserted that the cause of the recirculation zones was due to the negative buoyancy effects exerted on fuels with density greater than air. Since the density of methane is lower than that of air, due to a positive buoyancy effect, no recirculation zone has been formed. By contrast, propane is heavier than air and due to its higher relative density, a negative buoyancy effect causes recirculation zones along the centreline of the flame. The results from [111] raise the question if recirculation zones could be responsible for the complete conversion of ethane to soot observed in [13].

Since ethane has approximately the same density as air, there may be another mechanism that causes the observed recirculation zones in high pressure laminar diffusion flames. It should be noted that in the study by Xiong *et al.* [111], constant mass flow rates for air and for fuel were used for all flames, thus fuels with higher densities would have lower flow velocities. Other

researchers have noted the importance of selecting fuel and air mass flow rates such that the resultant flow velocities are matched to minimize shear effects [121, 122]; however, it is not known to what extent minimizing shear effects is necessary.

5.3 Agenda

In this present chapter, the CoFlame soot formation code [14], extensively validated at atmospheric pressure, and previously validated for soot volume fraction at elevated pressure against the data of Mandatori and Gülder [17], is utilized to investigate the potential of recirculation zones causing the observed complete conversion of ethane to soot. The influence of pressure on the size of any potential recirculation zones is explored, along with an explanation of the cause of the recirculation zone observed in this work and in [111].

5.4 Flame and Model Description

The flames chosen for this investigation are the steady, non-smoking, coflow laminar ethane/air diffusion flames at pressures of 2 to 33 atm, studied experimentally by Mandatori and Gülder [17, 92]. Fuel and air mass flow rates are kept constant as pressure is varied, with values of 0.0052 g/s for the fuel stream and 0.12 g/s for 15 atm and below, and 0.24 g/s at higher pressures for the air stream. The increased air mass flow rate at higher pressures was required to achieve stable flames in the experiments. The computational domain used extends 3.45 cm in the axial direction and 1.18 cm in the radial direction, and is divided into 416 (z) x 172 (r) control volumes. A non-uniform mesh is used to save computational cost while still resolving large spatial gradients. The first 0.5 cm in the z direction is below the fuel tube exit plane. This distance is sufficient to ensure the temperature gradients at $z = 0.0$ (the bottom of the computational domain) are negligible.

In order to validate the model, the methane-air, ethylene-air, and propane-air coflow laminar diffusion flames at atmospheric pressure studied by Xiong *et al*. [111] are simulated. The air flow velocity is 6.2 cm/s, with methane, ethylene, and propane flow velocities of 4.45, 2.21, and 1.40 cm/s, respectively. Therefore, the velocity ratio, or shear between the fuel and air streams, is not constant between the different fuels, with the propane-air case having a higher air-fuel velocity ratio. The computational domain used extends 12.54 cm in the axial direction and 3.95 cm in the radial direction, and is divided into 320 (z) x 135 (r) control volumes. The first 1.0 cm, 1.0 cm, and 2.0 cm in the z-direction is below the fuel tube exit plane for methane, ethylene, and propane, respectively. The distances are chosen to ensure the gradients at the inlet to the computational domain are near zero, and any further increase in the distance does not affect computational results. For the propane flame, a longer distance was required to ensure insensitivity to the amount of fuel tube included in the computational domain. For all flames, top-hat velocity profiles are utilized for the air and fuel stream boundary conditions.

For the gaseous phase, the fully coupled elliptical conservation equations for mass, momentum, energy, and species mass fraction are solved. CoFlame [14] utilizes the axi-symmetrical nature of the flame, and equations are solved in the two-dimensional (z and r) cylindrical co-ordinate system. Conjugate heat transfer between the solid fuel tube and the fuel and air streams is modelled using the harmonic mean method [23, 37]. The chemical kinetic mechanism that is used for this investigation is the one originally presented in [67], with modifications described in [21, 109].

Soot particle dynamics are described using a fixed sectional method in a same manner as in chapter 2 and chapter 3, in which soot particle mass ranges are divided logarithmically into 35 discrete sections. The soot sectional model includes several processes, those being nucleation,

PAH condensation, HACA surface growth, surface oxidation, coagulation, fragmentation, particle diffusion, and thermophoresis, and particle radiation are modelled in the same fashion as in [18-29, 83, 123]. A detailed description of the governing equations, boundary conditions, solution methodology, and chemical mechanism can be found in chapter 2 and chapter 3.

5.5 Results and Discussion

5.5.1 Flow Field Validation

Validation computations are performed for the methane-air, ethylene-air, and propane- air diffusion flames. Figure 5.1 displays the flow streamlines near the fuel tube exit plane for the methane-air (lowest fuel-air velocity ratio) on the left and the propane-air (highest fuel-air velocity ratio) on the right.

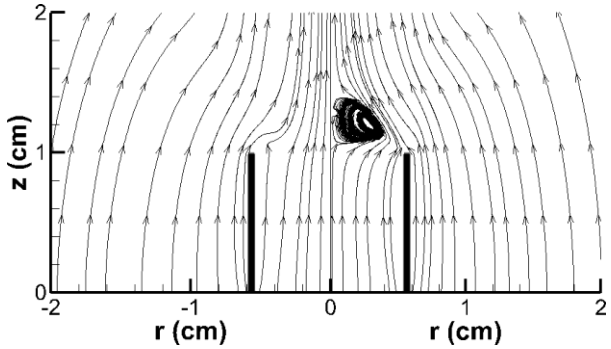

Figure 5.1: Computed flow streamlines by the CoFlame code near the fuel tube exit plane for an atmospheric methane-air diffusion flame on the left side, and an atmospheric propane-air flame on the right side.

The methane flame results display no recirculation zone, while the propane-air flame results display a recirculation zone along the center axis of the flame. Figure 5.1 demonstrates that the CoFlame model is able to capture the qualitative trend of the formation of a recirculation zone for propane, and non-formation for methane. Similar to the methane-air flame, no recirculation zone has been formed in the ethylene-air flame which can be explained due to a relatively close density

of ethylene to that of air. Only for the propane-air flame has a recirculation zone been observed, which is due to the denser nature of propane compared to air. To validate the qualitative results shown in Fig. 5.1, a comparison between the fuel velocity with respect to axial position along the centreline and to radial position at a constant height above the burner (z = 1 mm) has been provided in Fig. 5.2.

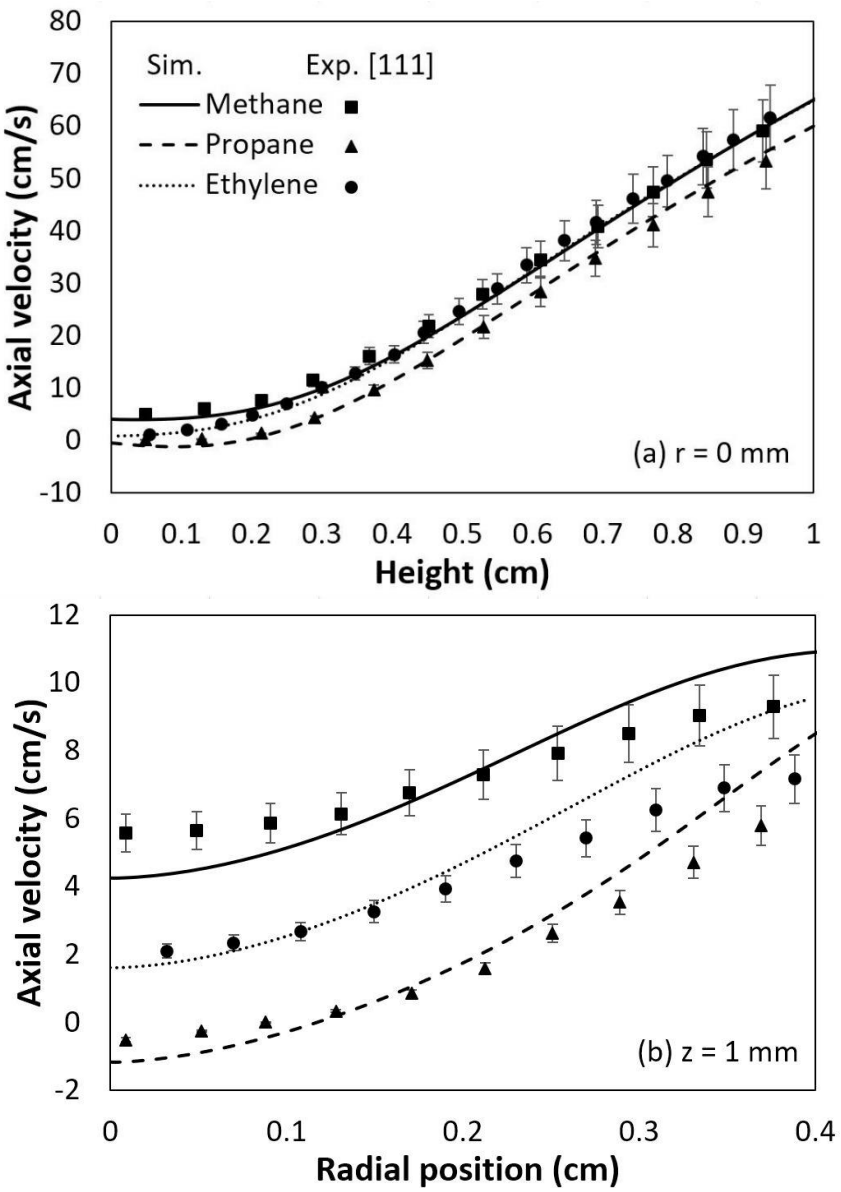

Figure 5.2: Comparison of the numerical and the experimental results of the axial (b: at r = 0 mm) and the radial profiles (a: at z = 1 mm) of the axial velocity for methane, ethylene, and propane flames

The CoFlame code predicts the same results as in [111]. The chemical mechanism was chosen to ensure model consistency across all flames. The propane sub-mechanism used in the present work could capture bulk combustion properties of diffusion flames. This sub-mechanism has been validated in the literature [124]. Further agreement is seen between simulation and experiment in the present work. Figure 5.2 demonstrates the capability of the CoFlame model in capturing the correct quantitative trend of the experimental results for both methane and propane [111].

5.5.2 Effect of Pressure on Flow Field

With the flow field predicted by the CoFlame code being validated, it is now applied to the ethane-air high pressure coflow diffusion flames. For flames at 10 atm and above, a flow phenomenon is computationally observed at the exit plane of the fuel tube near the centreline region. Figure 5.3 displays streamlines for the 10, 15, 20, 25, 30, and 33 atm flames, zoomed in near the exit of the fuel tube (black triangular region), which show the presence of a recirculation zone. This recirculation zone is not predicted at 2 atm or 5 atm flames; however, it is present for all other flames. It can be seen that the recirculation zone increases in size with increasing pressure. Additionally, as pressure increases, the streamlines near the fuel tube tip become increasingly more horizontal, directed towards the centreline of the flame. This is due to the thinning of the flame cross sectional area as pressure increases due to reductions in flame thickness with increasing pressure [22], thus the flow is accelerated inwards.

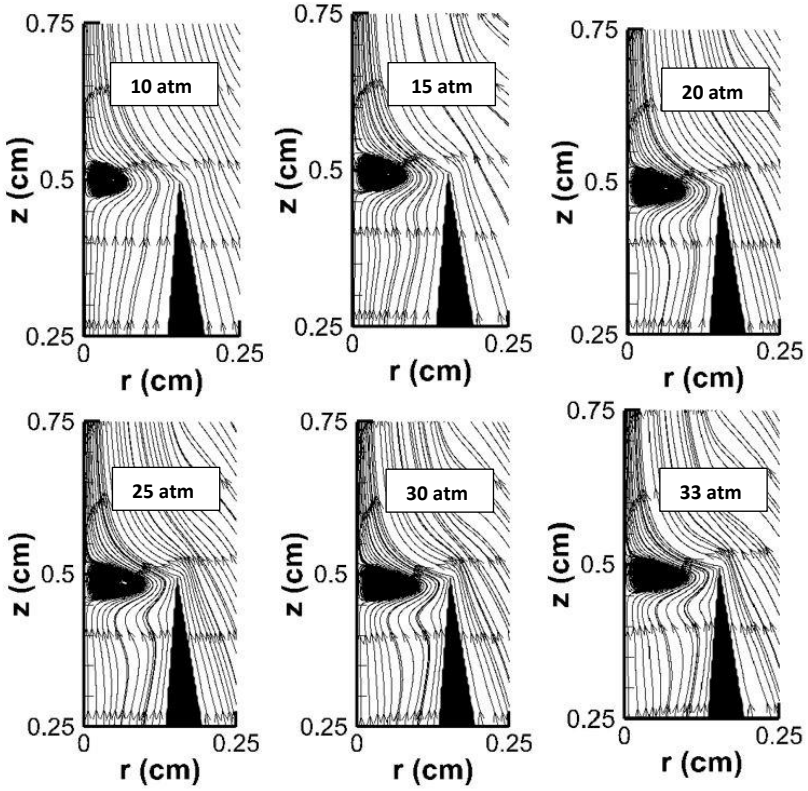

Figure 5.3: Computed flow streamlines with the CoFlame code near fuel tube tip for an ethane-air diffusion flame at 10 (top-left), 15 (top-middle), 20 (top-right), 25 (bottom- left), 30 (bottom-middle), and 33 (bottom-right) atm.

In order to gain an understanding as to why these recirculation zones were predicted, two cold flow cases (where no flame is present, and the entire domain is at 300 K), utilizing the inlet flow conditions for the 10 atm and 33 atm flame respectively, are computed. For the two cold flow cases, in which no flame is present, the recirculation zones do not appear. These results indicate that the recirculation zone is being predicted due to the influence of the high temperature flame on the flow field, which is consistent with the results in [111]. Table 5.1 displays the ratio of the air flow velocity to the fuel flow velocity at the exit plane of the fuel tube near the tube tip in both hot and cold cases. The velocity for the fuel and air is taken at a location that is sufficiently far away from the fuel tube to no longer be in the boundary layer. In the hot cases, as pressure is increased,

the ratio of air to fuel velocity increases. This result indicates that the shear between the air and fuel streams in the vicinity of the fuel tube increases with increasing pressure. The increase in the velocity ratio can be attributed to the high temperatures on the air side of the fuel tube (Ref. [23] displayed temperatures of approximately 1700-1800 K), causing the air velocity to increase. This effect is combined with the streamlines becoming more horizontal due to the change in flame cross sectional area, thus lowering the fuel velocity in the fuel tube tip region as well. The result is an increasing shear between the air and fuel streams as pressure increases. The increase in shear is accompanied by an increase in the size of the recirculation zone as well.

Table 5.1: Ratios of free-stream fluid velocity near fuel tube tip to average flow velocity in hot and cold cases

Pressure (atm)	**Velocity Ratio Hot Cases**	**Velocity Ratio Cold Cases**
2	2.12	1.83
5	3.00	1.91
10	3.42	2.05
15	3.88	2.25
20	7.92	4.06
25	8.36	4.22
30	8.88	4.30
33	9.36	4.36

Given these two analyses, the following assertion with regards to the cause of the recirculation zones is made. The recirculation zones are caused by the increasing acceleration of the air near the fuel tube tip as pressure increases, due to high temperatures, combined with the thinning of the flame cross sectional area and subsequent flattening of the flow streamlines. These two effects cause significant shear between the air and fuel streams, causing the fuel stream to accelerate in the region near the fuel tube tip. In order for continuity to be upheld, there must be a

corresponding deceleration of the fuel stream in the centreline region. Eventually, this required declaration is sufficiently large to cause the flow to reverse, and a recirculation zone forms.

Experimentally, it would be very difficult to detect the presence of these recirculation zones, as they are located in the centre of the flame, inside the fuel tube. This is contrary to the recirculation zones discovered in [111], as in that study the recirculation zones were fully above the exit plane of the fuel tube and thus detectable. It should be noted that while it would seem that simply reducing the air flow rate for experiments would reduce or eliminate the recirculation zones, there has to be consideration of flame stability as well. Most experiments at high pressure already utilized the minimum coflow air required to obtain a stable flame [11, 17, 92, 95, 114], thus eliminating these recirculation zones may not be possible in some cases.

Based on the role of shear in the presence of the recirculation zones, it should be possible to induce a recirculation zone simply by increasing the air flow velocity, or reducing the fuel flow velocity. Since in the experiments in [111] a constant mass flow rate was used for all fuels, the fuel flow velocity was smaller for heavier fuels (propane) than lighter fuels (methane). This means that for the heavier fuels, the shear between the air and fluid streams was higher, and thus the recirculation zones for the heavy fuel flames were influenced by the increased shear rather than directly due to the increases in the fuel density.

Another simulation is performed for the methane-air flame, except the air flow velocity is increased so that the ratio of the fuel to air velocities is the same as for the propane air case. For this simulation, a recirculation zone is not formed; however, upon increasing the air velocity by an additional factor of 2.25, a recirculation zone forms. This result supports the theory that the

recirculation zones are formed due to high local shear between the air and fuel fluid streams in the vicinity of the fuel tube.

5.5.3 Relationship Between Recirculation Zones and Soot Formation

To determine the relationship between the recirculation zones and soot formation, the 5 atm flame is re-simulated with the coflow air velocity increased by a factor of ten. This increase is sufficiently large to induce a recirculation zone, although not excessively large to induce turbulence (an increase by a factor of five did not induce a recirculation zone). Figure 5.4 displays the predicted soot volume fraction along the centreline of the flame with the experimental air flow rates and 10x the experimental rate and the experimental measurements [17]. There is a discrepancy between the experimental data and the computations at low axial heights; however, at heights below 0.5 cm, this can be attributed to the model not differentiating between nascent and mature soot. The experimental technique used to determine soot volume fraction is only sensitive to mature soot; however, the model lumps both nascent and mature soot into one entity [125]. Nascent soot tends to form in the lower temperature (less than 1300-1600 K) regions of flames, prior to formation of mature soot, thus the predicted large soot volume fraction at low axial heights is mostly nascent soot [45]. When the recirculation zone is present (10x case), there is an increase in soot volume fraction near the exit plane of the fuel tube (axial height 0.5 cm in the figure); however, at larger axial heights the difference between the peak soot volume fraction for the two cases is very minimal. In the experiment, the axial position of peak soot concentration is located at 0.65 cm above the burner. At this point, the experimental soot volume fraction is 81.6 ppm, while simulations with the regular and 10x air flow rate lead to the prediction of 75.1 and 77.1 ppm respectively, thus demonstrating the effect of the recirculation zone in increasing peak soot volume fraction along the centreline.

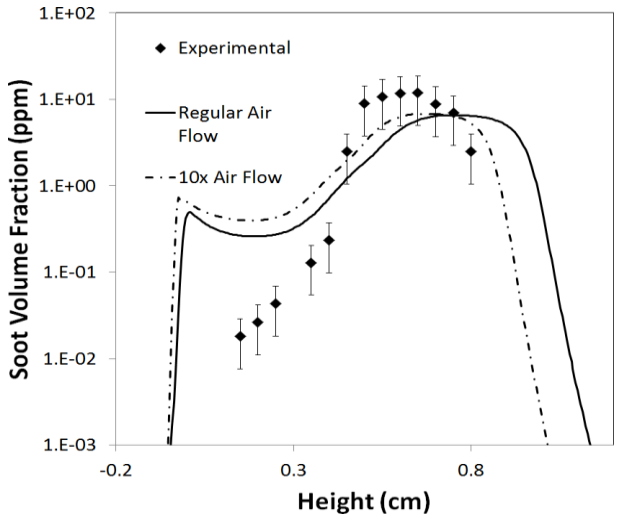

Figure 5.4: CoFlame computed centreline soot volume fraction profile compared with experimental data for ethane-air diffusion flames at 5 atm with experimental air flow rate and 10x the experimental flow rate. [9, 10]

It should be noted that as pressure increases, peak soot volume fraction rises. This growth in the value of maximum soot concentration is due to formation of recirculation zones, as well as an increase in pressure. Differentiation between the effect of the recirculation zone and pressure is of interest. Thus, simulations have been conducted with the air flow rate reduced by a factor of 2 and 4 at 10, 15, and 20 atm flames in an attempt to remove recirculation zones and study the effect of only pressure on soot concentration. Reducing the air flow rate at the mentioned simulations did not remove the recirculation zone. A limitation for reducing the air flow rate is the stability of the flame, which was jeopardized when applying a reduction factor more than 4. Therefore, further differentiation between the effect of recirculation and pressure was not possible in the present study. Differentiation between the effect of the recirculation zone and pressure was restricted to manipulating the 5 atm flame, in an attempt to add the recirculation effect to it, as shown in Fig. 5.4.

Figure 5.5 displays the predicted soot volume fraction along the centreline of the 10 and

33 atm ethane-air flames with the experimental air flow rates and the experimental measurements [17]. It can be seen that the calculations for the 33 atm flame correctly predict a higher soot volume fraction in the recirculation zone than for the 10 atm flame. As pressure is increased, the size of the recirculation zone increases, and a larger soot volume fraction is predicted in the zone. The results point to an explanation for the experimentally observed complete conversion of the flame to soot at 36.5 atm [13]. Calculations for the 36.5 atm flame were attempted; however, a converged solution could not be obtained. Prior to divergence, the predicted recirculation zone spanned the entirety of the fuel tube exit plane with a very large ($O(10^3)$ ppm) soot volume fraction in the zone, which eventually lead to divergence. This leads to the assertion that the complete conversion to soot is caused by the recirculation zone. While the CoFlame code is not a transient solver, nor can it handle bulk solid phases, the trend of increasing soot in the recirculation zone as pressure increases and being unable to obtain a converged solution for the 36.5 atm flame support the stated assertion. To summarize, the effect of the recirculation zones on centreline soot formation is minimal up until the point the zone is sufficiently large to cause a complete conversion to soot.

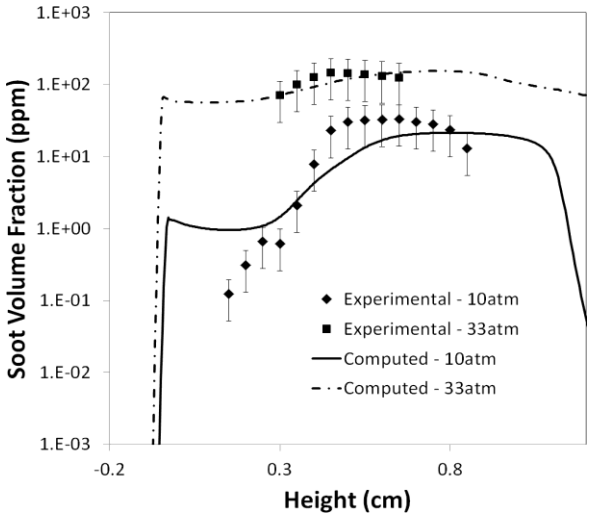

Figure 5.5: CoFlame computed centreline soot volume fraction profile compared with experimental data for ethane-air diffusion flames at 10 and 33 atm with experimental air flow rate. [9, 10]

5.6 Summary

The effect of pressure on near nozzle flow field and soot formation in laminar diffusion flames is investigated numerically using the CoFlame code. The code is validated against previous experimental data for methane and propane diffusion flames in its ability to correctly predict the formation of recirculation zones. From 10 atm and greater, recirculation zones are predicted to form along the centreline of the flame near the exit plane of the fuel tube for ethane-air diffusion flames previously experimentally and numerically investigated. The recirculation zones are shown to be caused by the increased local shear between the fuel and air fluid streams, and not solely due to density differences between the fuel and air. The formed recirculation zones are therefore able to explain the experimentally observed complete conversion of ethane to soot at 36.5 atm, although the effect of the recirculation zones on soot formation is shown to be minimal otherwise. Future work should focus on verifying the effect of shear experimentally for atmospheric diffusion flames where the recirculation zone would be more easily detected.

Chapter 6 – Closure

6.1 Summary and Conclusions

In this project, a detailed numerical soot formation code has been successfully utilized to model varying-pressure coflow laminar diffusion flames. The code uses a detailed soot formation model, including a detailed gas phase mechanism and soot aerosol dynamics model. This thesis has two parts; first, investigation of the impact of a more predictive temperature-history dependent functional form for soot surface reactivity coupled with a novel pressure-based model on soot concentration, presented in chapter 4, and second, assessment of the influence of pressure on the flow field and the subsequent effect of the flow field on soot formation in elevated-pressure coflow diffusion flames, addressed in chapter 5. In the following paragraphs, major findings of each study presented in this dissertation are summarized.

In chapter 4, the soot surface reactivity function proposed by Khosousi and Dworkin [12] is employed in modelling varying-pressure coflow diffusion flames using the CoFlame code. It is based on the temperature history of soot particles. Although this function was very successful in modelling different experimental data sets at atmospheric pressure, the disparity between simulation and experiment rises as pressure increases. One reason for this discrepancy could be explained by the fact that chemical reaction rates for the soot growth mechanism at atmospheric combustion do not adequately characterize higher pressures. Therefore, a new pressure-based acetylene addition reaction rate for the soot growth mechanism has been coupled with a functional surface reactivity model. It resulted in increasing the soot concentration at the wing regions as pressure rises. However, the quantity for soot concentration along the centerline is nearly

independent of the surface reactivity model chosen and it needs further investigation. The present model is capable of capturing qualitative trends along both wing regions and centerline of the flame.

In chapter 5, the effect of pressure on the near nozzle flow field in soot formation in coflow laminar diffusion flames has been investigated numerically using the CoFlame code. First, the code was validated against previous experimental data in its ability to correctly predict the formation of recirculation zones. After validation, simulations showed that from 10 atm and greater, recirculation zones are predicted to form along the centerline of the flame near the exit plane of the fuel tube for ethane-air diffusion flames previously experimentally and numerically investigated. The recirculation zones are shown to be caused by the increased local shear between the fuel and air fluid streams. The formed recirculation zones are therefore able to explain the experimentally observed complete conversion of ethane to soot at 36.5 atm, in which no adequate explanation for the formation of the large mass of soot existed.

6.2 Recommendations for Future Work

Soot formation is a very complex subject and still poorly understood. More experimental and numerical studies are required to gain a better understanding of soot formation mechanics, especially at elevated pressures. Considering the detailed modelling of soot formation at varying-pressure combustion performed in this thesis, the following recommendations are suggested for future studies:

1. Regarding the soot surface reactivity model combined with the new pressure-based reaction rate, the objective of future work should be implementing this model in different laminar diffusion flames, premixed flames, and also various burner configurations for investigating the

applicability of this model in other combustion systems. Moreover, investigation of the impact of this model on inception and condensation rates would be an interesting topic.

2. As pressure increases, PAH condensation becomes more dominant than HACA and plays a significant role in the total mass added to soot particles. Although there are some numerical studies on effects of PAH condensation on soot formation in atmospheric combustion, more experimental and numerical assessments are required, particularly at elevated pressures. Due to the high importance of PAH condensation at higher pressures, studies should fully characterize the nature of this phenomenon. Also, more experimental studies need to be performed for validation purposes.

3. The project described in chapter 5 showed that the recirculation zone due to increases in shear is determined as a probable cause of the experimentally observed formation of a large mass of soot covering the entire fuel tube exit for an ethane diffusion flame at 36.5 atm. Future work should focus on verifying the effect of shear experimentally for atmospheric diffusion flames where the recirculation zone would be more easily detected. Another interesting experimental data set to study is the methane-oxygen coflow laminar diffusion flame at pressures up to 100 atm, conducted by Joo and Gülder [11], in which soot volume fraction reaches a peak at 55 atm, then declines as pressure is raised further. It is recommended to conduct numerical simulation on this data set in order to assess the reason of this phenomenon and also to better understand the impact of pressure on soot concentration.

4. The other project would be improvement of the code efficiency which allows obtaining numerical results faster and more efficiently. Moreover, since the end goal of studying soot formation mechanics is applying that in industrial applications of combustion which are mostly

turbulent, improving the code's parallel efficiency would increase the feasibility of the detailed soot model for simulating turbulent flames.

Bibliography

[1] International Energy Agency, World Energy Outlook, (2018).
[2] M.Z. Jacobson, Strong radiative heating due to the mixing state of black carbon in atmospheric aerosols, Nature 409 (2001) 695-697.
[3] Climate change and health, World Health Organization, (2018).
[4] F. Xu, K.C. Lin, G.M. Faeth, Soot Formation in Laminar Premixed Methane/Oxygen Flames at Atmospheric Pressure, Combustion and Flame 115 (1998) 195-209.
[5] M. Williams, R. Minjares, A technical summary of Euro 6/VI vehicle emission standards, (2016).
[6] B.S. Haynes, H.G. Wagner, Soot formation, Prog. Energy Combust. Sci. 7 (1981) 229-273.
[7] H. Bockhorn, Soot Formation in Combustion: Mechanisms and Models, Springer-Verlag, (1994).
[8] J. Appel, H. Bockhorn, M. Frenklach, Kinetic modeling of soot formation with detailed chemistry and physics: laminar premixed flames of C2 hydrocarbons, Combustion and Flame 121 (2000) 122-136.
[9] I.M. Kennedy, C. Yam, D.C. Rapp, R.J. Santoro, Modeling and measurements of soot and species in a laminar diffusion flame, Combustion and Flame 107 (1996) 368-382.
[10] H.I. Joo, Ö.L. Gülder, Soot formation and temperature field structure in co-flow laminar methane–air diffusion flames at pressures from 10 to 60atm, Proceedings of the Combustion Institute 32 (2009) 769-775.
[11] H.I. Joo, Ö.L. Gülder, Soot formation and temperature structure in small methane–oxygen diffusion flames at subcritical and supercritical pressures, Combustion and Flame 157 (2010) 1194-1201.
[12] A. Khosousi, S.B. Dworkin, Soot surface reactivity during surface growth and oxidation in laminar diffusion flames, Combust. Flame 162 (2015) 4523-4532.
[13] P.M. Mandatori, Ö.L. Gülder, Complete conversion of ethane to soot in a coflow laminar diffusion flame at 3.65 MPa, Combustion and Flame 150 (2007) 400-403.
[14] N.A. Eaves, Q. Zhang, F. Liu, H. Guo, S.B. Dworkin, M.J. Thomson, CoFlame: A refined and validated numerical algorithm for modeling sooting laminar coflow diffusion flames, Computer Physics Communications 207 (2016) 464-477.
[15] A.E. Karataş, Ö.L. Gülder, Dependence of sooting characteristics and temperature field of co-flow laminar pure and nitrogen-diluted ethylene–air diffusion flames on pressure, Combustion and Flame 162 (2015) 1566-1574.
[16] A. Bennett, H.M.F. Amin, E. Cenker, W.L. Roberts, Measurements of Pressure Effects on PAH Distribution and 2D Soot Volume Fraction Diagnostics in a Laminar Non-premixed Coflow Flame, Energy & Fuels 32 (2018) 10974-10983.
[17] P.M. Mandatori, Ö.L. Gülder, Soot formation in laminar ethane diffusion flames at pressures from 0.2 to 3.3MPa, Proceedings of the Combustion Institute 33 (2011) 577-584.
[18] V. Chernov, M.J. Thomson, S.B. Dworkin, N.A. Slavinskaya, U. Riedel, Soot formation with C1 and C2 fuels using an improved chemical mechanism for PAH growth, Combust. Flame 161 (2014) 592-601.
[19] Q. Zhang, H. Guo, F. Liu, G.J. Smallwood, M.J. Thomson, Modeling of soot aggregate formation and size distribution in a laminar ethylene/air coflow diffusion flame with detailed

PAH chemistry and an advanced sectional aerosol dynamics model, Proceedings of the Combustion Institute 32 (2009) 761-768.
[20] Q. Zhang, H. Guo, F. Liu, G.J. Smallwood, M.J. Thomson, Implementation of an advanced fixed sectional aerosol dynamics model with soot aggregate formation in a laminar methane/air coflow diffusion flame, Combust. Theor. Model. 12 (2008) 621-641.
[21] S.B. Dworkin, Q. Zhang, M.J. Thomson, N.A. Slavinskaya, U. Riedel, Application of an enhanced PAH growth model to soot formation in a laminar coflow ethylene/air diffusion flame, Combustion and Flame 158 (2011) 1682-1695.
[22] N.A. Eaves, A. Veshkini, C. Riese, Q. Zhang, S.B. Dworkin, M.J. Thomson, A numerical study of high pressure, laminar, sooting, ethane–air coflow diffusion flames, Combust. Flame 159 (2012) 3179-3190.
[23] N.A. Eaves, M.J. Thomson, S.B. Dworkin, The Effect of Conjugate Heat Transfer on Soot Formation Modeling at Elevated Pressures, Combust. Sci. Technol. 185 (2013) 1799-1819.
[24] M. Saffaripour, M. Kholghy, S.B. Dworkin, M.J. Thomson, A numerical and experimental study of soot formation in a laminar coflow diffusion flame of a Jet A-1 surrogate, Proceedings of the Combustion Institute 34 (2013) 1057-1065.
[25] V. Chernov, Q. Zhang, M.J. Thomson, S.B. Dworkin, Numerical investigation of soot formation mechanisms in partially-premixed ethylene–air co-flow flames, Combustion and Flame 159 (2012) 2789-2798.
[26] N.A. Eaves, S.B. Dworkin, M.J. Thomson, The importance of reversibility in modeling soot nucleation and condensation processes, Proceedings of the Combustion Institute 35 (2015) 1787-1794.
[27] A. Veshkini, S.B. Dworkin, M.J. Thomson, A soot particle surface reactivity model applied to a wide range of laminar ethylene/air flames, Combust. Flame 161 (2014) 3191-3200.
[28] M. Saffaripour, A. Veshkini, M. Kholghy, M.J. Thomson, Experimental investigation and detailed modeling of soot aggregate formation and size distribution in laminar coflow diffusion flames of Jet A-1, a synthetic kerosene, and n-decane, Combust. Flame 161 (2014) 848-863.
[29] A. Khosousi, S.B. Dworkin, Detailed modelling of soot oxidation by O2 and OH in laminar diffusion flames, Proc. Combust. Inst. 35 (2015) 1903-1910.
[30] A. Gomez, D.E. Rosner, Thermophoretic Effects on Particles in Counterflow Laminar Diffusion Flames, Combustion Science and Technology 89 (1993) 335-362.
[31] F. Liu, G.J. Smallwood, Oslash, m.L. G-uacute, lder, Band Lumping Strategy for Radiation Heat Transfer Calculations Using a Narrowband Model, Journal of Thermophysics and Heat Transfer 14 (2000) 278-281.
[32] K.H. Lee, R. Viskanta, Prediction of spectral radiative transfer in a condensed cylindrical medium using discrete ordinates method, Journal of Quantitative Spectroscopy and Radiative Transfer 58 (1997) 329-345.
[33] C.P. Thurgood, A. Pollard, H.A. Becker, The TN Quadrature Set for the Discrete Ordinates Method, Journal of Heat Transfer 117 (1995) 1068-1070.
[34] F. Liu, Numerical Solutions of Three-Dimensional Non-Grey Gas Radiative Transfer Using the Statistical Narrow-Band Model, Journal of Heat Transfer 121 (1999) 200-203.
[35] F. Liu, Ö.L. Gülder, G.J. Smallwood, Y. Ju, Non-grey gas radiative transfer analyses using the statistical narrow-band model, International Journal of Heat and Mass Transfer 41 (1998) 2227-2236.

[36] K.A. Thomson, Ö.L. Gülder, E.J. Weckman, R.A. Fraser, G.J. Smallwood, D.R. Snelling, Soot concentration and temperature measurements in co-annular, nonpremixed CH4/air laminar flames at pressures up to 4 MPa, Combustion and Flame 140 (2005) 222-232.
[37] S.V. Patankar, Numerical Heat Transfer and Fluid Flow, Hemisphere, New York (1980).
[38] R. Kee, J. Miller, T. Jefferson, Chemkin: A General Purpose, Problem Independent, Transportable, Fortran Chemical Kinetics Code Package, Technical Report SAN80-8003, Sandia (1980),
[39] R. Kee, F. Rupley, J. Miller, A Fortran Chemical Kinetics Package for the Analysis of Gas-phase Chemical Kinetics, Technical Report SAN89-8009, Sandia, (1989).
[40] W. Gropp, R. Thakur, E. Lusk, Using MPI-2: Advanced Features of the Message Passing Interface, MIT Press1999.
[41] A. Toselli, O. Widlund, Domain Decomposition Methods - Algorithms and Theory, Springer Berlin Heidelberg2004.
[42] C.P. Arana, M. Pontoni, S. Sen, I.K. Puri, Field measurements of soot volume fractions in laminar partially premixed coflow ethylene/air flames, Combustion and Flame 138 (2004) 362-372.
[43] R.A. Dobbins, C.M. Megaridis, Morphology of flame-generated soot as determined by thermophoretic sampling, Langmuir 3 (1987) 254-259.
[44] S.S. Iyer, T.A. Litzinger, S.-Y. Lee, R.J. Santoro, Determination of soot scattering coefficient from extinction and three-angle scattering in a laminar diffusion flame, Combustion and Flame 149 (2007) 206-216.
[45] M. Kholghy, M. Saffaripour, C. Yip, M.J. Thomson, The evolution of soot morphology in a laminar coflow diffusion flame of a surrogate for Jet A-1, Combustion and Flame 160 (2013) 2119-2130.
[46] Ü.Ö. Köylü, C.S. McEnally, D.E. Rosner, L.D. Pfefferle, Simultaneous measurements of soot volume fraction and particle size / microstructure in flames using a thermophoretic sampling technique, Combust. Flame 110 (1997) 494-507.
[47] C.S. McEnally, Ü.Ö. Köylü, L.D. Pfefferle, D.E. Rosner, Soot volume fraction and temperature measurements in laminar nonpremixed flames using thermocouples, Combust. Flame 109 (1997) 701-720.
[48] M.D. Smooke, C.S. McEnally, L.D. Pfefferle, R.J. Hall, M.B. Colket, Computational and experimental study of soot formation in a coflow, laminar diffusion flame, Combustion and Flame 117 (1999) 117-139.
[49] M.D. Smooke, M. Long, B. Connelly, M. Colket, R. Hall, Soot formation in laminar diffusion flames, Combust. Flame 143 (2005) 613-628.
[50] C. Russo, F. Stanzione, A. Tregrossi, M. Alfè, A. Ciajolo, The effect of temperature on the condensed phases formed in fuel-rich premixed benzene flames, Combustion and Flame 159 (2012) 2233-2242.
[51] C. Russo, M. Alfè, J.-N. Rouzaud, F. Stanzione, A. Tregrossi, A. Ciajolo, Probing structures of soot formed in premixed flames of methane, ethylene and benzene, Proceedings of the Combustion Institute 34 (2013) 1885-1892.
[52] M. Alfè, B. Apicella, J.N. Rouzaud, A. Tregrossi, A. Ciajolo, The effect of temperature on soot properties in premixed methane flames, Combustion and Flame 157 (2010) 1959-1965.
[53] J. Camacho, C. Liu, C. Gu, H. Lin, Z. Huang, Q. Tang, X. You, C. Saggese, Y. Li, H. Jung, L. Deng, I. Wlokas, H. Wang, Mobility size and mass of nascent soot particles in a benchmark premixed ethylene flame, Combustion and Flame 162 (2015) 3810-3822.

[54] A. D'Anna, M. Commodo, S. Violi, C. Allouis, J. Kent, Nano organic carbon and soot in turbulent non-premixed ethylene flames, Proceedings of the Combustion Institute 31 (2007) 621-629.
[55] G.M. Faeth, Ü.Ö. KÖYlÜ, Soot Morphology and Optical Properties in Nonpremixed Turbulent Flame Environments, Combustion Science and Technology 108 (1995) 207-229.
[56] N.H. Qamar, G.J. Nathan, Z.T. Alwahabi, K.D. King, The effect of global mixing on soot volume fraction: measurements in simple jet, precessing jet, and bluff body flames, Proceedings of the Combustion Institute 30 (2005) 1493-1500.
[57] B. Hu, B. Yang, Ü.Ö. Köylü, Soot measurements at the axis of an ethylene/air non-premixed turbulent jet flame, Combust. Flame 134 (2003) 93-106.
[58] R.A. Dobbins, R.A. Fletcher, H.C. Chang, The evolution of soot precursor particles in a diffusion flame, Combust. Flame 115 (1998) 285-298.
[59] R.A. Dobbins, Hydrocarbon Nanoparticles Formed in Flames and Diesel Engines, Aerosol Science and Technology 41 (2007) 485-496.
[60] Ü.Ö. Köylü, G.M. Faeth, T.L. Farias, M.G. Carvalho, Fractal and projected structure properties of soot aggregates, Combustion and Flame 100 (1995) 621-633.
[61] B. Hu, Ü.Ö. Köylü, Size and Morphology of Soot Particulates Sampled from a Turbulent Nonpremixed Acetylene Flame, Aerosol Science and Technology 38 (2004) 1009-1018.
[62] R. Puri, T.F. Richardson, R.J. Santoro, R.A. Dobbins, Aerosol dynamic processes of soot aggregates in a laminar ethene diffusion flame, Combust. Flame 92 (1993) 320-333.
[63] M. Frenklach, D.W. Clary, W.C. Gardiner, S.E. Stein, Detailed kinetic modeling of soot formation in shock-tube pyrolysis of acetylene, Symposium (International) on Combustion 20 (1985) 887-901.
[64] J.A. Miller, C.F. Melius, Kinetic and thermodynamic issues in the formation of aromatic compounds in flames of aliphatic fuels, Combustion and Flame 91 (1992) 21-39.
[65] C.F. Melius, M.E. Colvin, N.M. Marinov, W.J. Pit, S.M. Senkan, Reaction mechanisms in aromatic hydrocarbon formation involving the C5H5 cyclopentadienyl moiety, Symposium (International) on Combustion 26 (1996) 685-692.
[66] Gregory P. Smith, David M. Golden, Michael Frenklach, Nigel W. Moriarty, Boris Eiteneer, Mikhail Goldenberg, C. Thomas Bowman, Ronald K. Hanson, Soonho Song, William C. Gardiner, Jr., Vitali V. Lissianski, and Zhiwei Qin http://www.me.berkeley.edu/gri_mech/.
[67] N.A. Slavinskaya, P. Frank, A modelling study of aromatic soot precursors formation in laminar methane and ethene flames, Combustion and Flame 156 (2009) 1705-1722.
[68] N.M. Marinov, W.J. Pitz, C.K. Westbrook, A.M. Vincitore, M.J. Castaldi, S.M. Senkan, C.F. Melius, Aromatic and Polycyclic Aromatic Hydrocarbon Formation in a Laminar Premixed n-Butane Flame, Combustion and Flame 114 (1998) 192-213.
[69] H. Wang, Formation of nascent soot and other condensed-phase materials in flames, Proceedings of the Combustion Institute 33 (2011) 41-67.
[70] K.-H. Homann, Fullerenes and Soot Formation— New Pathways to Large Particles in Flames, Angewandte Chemie International Edition 37 (1998) 2434-2451.
[71] M. Frenklach, Reaction mechanism of soot formation in flames, Physical Chemistry Chemical Physics 4 (2002) 2028-2037.
[72] M. Frenklach, H. Wang, Detailed modeling of soot particle nucleation and growth, Symposium (International) on Combustion 23 (1991) 1559-1566.
[73] A. D'Anna, Combustion-formed nanoparticles, Proceedings of the Combustion Institute 32 (2009) 593-613.

[74] S.H. Park, S.N. Rogak, W.K. Bushe, J.Z. Wen, M.J. Thomson, An aerosol model to predict size and structure of soot particles, Combustion Theory and Modelling 9 (2005) 499-513.
[75] J.Z. Wen, M.J. Thomson, M.F. Lightstone, S.N. Rogak, Detailed Kinetic Modeling of Carbonaceous Nanoparticle Inception and Surface Growth during the Pyrolysis of C6H6 behind Shock Waves, Energy & Fuels 20 (2006) 547-559.
[76] J.Z. Wen, M.J. Thomson, M.F. Lightstone, S.H. Park, S.N. Rogak, AN IMPROVED MOVING SECTIONAL AEROSOL MODEL OF SOOT FORMATION IN A PLUG FLOW REACTOR, Combustion Science and Technology 178 (2006) 921-951.
[77] J.Z. Wen, M.J. Thomson, S.H. Park, S.N. Rogak, M.F. Lightstone, Study of soot growth in a plug flow reactor using a moving sectional model, Proceedings of the Combustion Institute 30 (2005) 1477-1484.
[78] Q. Zhang, Detailed modeling of soot formation/oxidation in laminar coflow diffusion flames, University of Toronto, Toronto, Canada, 2009.
[79] S.N. Rogak, R.C. Flagan, Coagulation of aerosol agglomerates in the transition regime, Journal of Colloid and Interface Science 151 (1992) 203-224.
[80] C.M. Sorensen, G.M. Wang, Note on the Correction for Diffusion and Drag in the Slip Regime, Aerosol Science and Technology 33 (2000) 353-356.
[81] K.-H. Naumann, COSIMA—a computer program simulating the dynamics of fractal aerosols, Journal of Aerosol Science 34 (2003) 1371-1397.
[82] S.H. Park, S.N. Rogak, A novel fixed-sectional model for the formation and growth of aerosol agglomerates, Journal of Aerosol Science 35 (2004) 1385-1404.
[83] Q. Zhang, M.J. Thomson, H. Guo, F. Liu, G.J. Smallwood, Modeling of Oxidation-Driven Soot Aggregate Fragmentation in a Laminar Coflow Diffusion Flame, Combust. Sci. Technol. 182 (2010) 491-504.
[84] S.J. Harris, M.M. Maricq, The role of fragmentation in defining the signature size distribution of diesel soot, Journal of Aerosol Science 33 (2002) 935-942.
[85] M. Frenklach, R.I. Singh, A.M. Mebel, On the low-temperature limit of HACA, Proceedings of the Combustion Institute 37 (2019) 969-976.
[86] R.J. Santoro, T.T. Yeh, J.J. Horvath, H.G. Semerjian, The Transport and Growth of Soot Particles in Laminar Diffusion Flames, Combustion Science and Technology 53 (1987) 89-115.
[87] Q. Zhang, M.J. Thomson, H. Guo, F. Liu, G.J. Smallwood, A numerical study of soot aggregate formation in a laminar coflow diffusion flame, Combustion and Flame 156 (2009) 697-705.
[88] (!!! INVALID CITATION !!! [88-91]).
[89] A.E. Karataş, Ö.L. Gülder, Effects of carbon dioxide and nitrogen addition on soot processes in laminar diffusion flames of ethylene-air at high pressures, Fuel 200 (2017) 76-80.
[90] A.M. Vargas, Ö.L. Gülder, Pressure dependence of primary soot particle size determined using thermophoretic sampling in laminar methane-air diffusion flames, Proceedings of the Combustion Institute 36 (2017) 975-984.
[91] L.L. McCrain, W.L. Roberts, Measurements of the soot volume field in laminar diffusion flames at elevated pressures, Combustion and Flame 140 (2005) 60-69.
[92] P.M. Mandatori, Soot Formation in Ethane-air Coflow Laminar Diffusion Flames at Elevated Pressures, Library and Archives Canada = Bibliothèque et Archives Canada2006.
[93] A.E. Karataş, Ö.L. Gülder, Soot formation in high pressure laminar diffusion flames, Progress in Energy and Combustion Science 38 (2012) 818-845.

[94] P.H. Joo, B. Gigone, E.A. Griffin, M. Christensen, Ö.L. Gülder, Soot primary particle size dependence on combustion pressure in laminar ethylene diffusion flames, Fuel 220 (2018) 464-470.
[95] H.I. Joo, Ö.L. Gülder, Experimental study of soot and temperature field structure of laminar co-flow ethylene–air diffusion flames with nitrogen dilution at elevated pressures, Combustion and Flame 158 (2011) 416-422.
[96] H. Guo, Z. Gu, K.A. Thomson, G.J. Smallwood, F.F. Baksh, Soot formation in a laminar ethylene/air diffusion flame at pressures from 1 to 8atm, Proceedings of the Combustion Institute 34 (2013) 1795-1802.
[97] Ö.L. Gülder, G. Intasopa, H.I. Joo, P.M. Mandatori, D.S. Bento, M.E. Vaillancourt, Unified behaviour of maximum soot yields of methane, ethane and propane laminar diffusion flames at high pressures, Combustion and Flame 158 (2011) 2037-2044.
[98] E.A. Griffin, Ö.L. Gülder, Soot formation in diluted laminar ethene, propene and 1-butene diffusion flames at elevated pressures, Combustion and Flame 197 (2018) 378-388.
[99] E.A. Griffin, M. Christensen, Ö.L. Gülder, Effect of ethanol addition on soot formation in laminar methane diffusion flames at pressures above atmospheric, Combustion and Flame 193 (2018) 306-312.
[100] B. Gigone, A.E. Karataş, Ö.L. Gülder, Soot aggregate morphology in coflow laminar ethylene diffusion flames at elevated pressures, Proceedings of the Combustion Institute 37 (2019) 841-848.
[101] M. Commodo, P.H. Joo, G. De Falco, P. Minutolo, A. D'Anna, Ö.L. Gülder, Raman Spectroscopy of Soot Sampled in High-Pressure Diffusion Flames, Energy & Fuels 31 (2017) 10158-10164.
[102] M.R.J. Charest, C.P.T. Groth, Ö.L. Gülder, A numerical study on the effects of pressure and gravity in laminar ethylene diffusion flames, Combustion and Flame 158 (2011) 1933-1945.
[103] M.R.J. Charest, C.P.T. Groth, Ö.L. Gülder, Effects of gravity and pressure on laminar coflow methane–air diffusion flames at pressures from 1 to 60 atmospheres, Combustion and Flame 158 (2011) 860-875.
[104] F. Liu, A.E. Karataş, Ö.L. Gülder, M. Gu, Numerical and experimental study of the influence of CO2 and N2 dilution on soot formation in laminar coflow C2H4/air diffusion flames at pressures between 5 and 20atm, Combust. Flame 162 (2015) 2231-2247.
[105] J.B. Howard, Carbon addition and oxidation reactions in heterogeneous combustion and soot formation, Symposium (International) on Combustion 23 (1991) 1107-1127.
[106] I. Cherchneff, The formation of polycyclic aromatic hydrocarbons in evolved circumstellar environments, (2011).
[107] C.J. Dasch, The decay of soot surface growth reactivity and its importance in total soot formation, Combust. Flame 61 (1985) 219-225.
[108] M. Alfè, B. Apicella, R. Barbella, J.N. Rouzaud, A. Tregrossi, A. Ciajolo, Structure–property relationship in nanostructures of young and mature soot in premixed flames, Proc. Combust. Inst. 32 (2009) 697-704.
[109] N.A. Slavinskaya, U. Riedel, S.B. Dworkin, M.J. Thomson, Detailed numerical modeling of PAH formation and growth in non-premixed ethylene and ethane flames, Combust. Flame 159 (2012) 979-995.
[110] S.R. Turns, An Introduction to Combustion: Concepts and Applications, McGraw-Hill2012.

[111] Y. Xiong, M.S. Cha, S.H. Chung, Fuel density effect on near nozzle flow field in small laminar coflow diffusion flames, Proceedings of the Combustion Institute 35 (2015) 873-880.
[112] W.L. Flower, C.T. Bowman, Soot production in axisymmetric laminar diffusion flames at pressures from one to ten atmospheres, Symposium (International) on Combustion 21 (1988) 1115-1124.
[113] W. Lee, Y.D. Na, Soot Study in Laminar Diffusion Flames at Elevated Pressure Using Two-Color Pyrometry and Abel Inversion, JSME International Journal Series B 43 (2000) 550-555.
[114] D.S. Bento, K.A. Thomson, Ö.L. Gülder, Soot formation and temperature field structure in laminar propane–air diffusion flames at elevated pressures, Combustion and Flame 145 (2006) 765-778.
[115] A.E. Karataş, G. Intasopa, Ö.L. Gülder, Sooting behaviour of n-heptane laminar diffusion flames at high pressures, Combustion and Flame 160 (2013) 1650-1656.
[116] M.R.J. Charest, Ö.L. Gülder, C.P.T. Groth, Numerical and experimental study of soot formation in laminar diffusion flames burning simulated biogas fuels at elevated pressures, Combustion and Flame 161 (2014) 2678-2691.
[117] F. Liu, K.A. Thomson, H. Guo, G.J. Smallwood, Numerical and experimental study of an axisymmetric coflow laminar methane–air diffusion flame at pressures between 5 and 40 atmospheres, Combustion and Flame 146 (2006) 456-471.
[118] M.R.J. Charest, H.I. Joo, Ö.L. Gülder, C.P.T. Groth, Experimental and numerical study of soot formation in laminar ethylene diffusion flames at elevated pressures from 10 to 35atm, Proceedings of the Combustion Institute 33 (2011) 549-557.
[119] M.R.J. Charest, C.P.T. Groth, Ö.L. Gülder, A computational framework for predicting laminar reactive flows with soot formation, Combust. Theor. Model. 14 (2010) 793-825.
[120] M.R.J. Charest, Numerical Modelling of Sooting Laminar Diffusion Flames at Elevated Pressures and Microgravity, Aerospace Science and Engineering, University of Toronto, 2010.
[121] M.D. Smooke, M.B. Long, B.C. Connelly, M.B. Colket, R.J. Hall, Soot formation in laminar diffusion flames, Combust. Flame 143 (2005) 613-628.
[122] R.K. Abhinavam Kailasanathan, J. Zhang, T. Fang, W.L. Roberts, Effects of Diluents on Soot Surface Temperature and Volume Fraction in Diluted Ethylene Diffusion Flames at Pressure, Combustion Science and Technology 186 (2014) 815-828.
[123] F. Liu, S.B. Dworkin, M.J. Thomson, G.J. Smallwood, Modeling DME Addition Effects to Fuel on PAH and Soot in Laminar Coflow Ethylene/Air Diffusion Flames Using Two PAH Mechanisms, Combust. Sci. Technol. 184 (2012) 966-979.
[124] K.M. Leung, R.P. Lindstedt, Detailed kinetic modeling of C1 — C3 alkane diffusion flames, Combust. Flame 102 (1995) 129-160.
[125] M.R. Kholghy, J. Weingarten, M.J. Thomson, A study of the effects of the ester moiety on soot formation and species concentrations in a laminar coflow diffusion flame of a surrogate for B100 biodiesel, Proceedings of the Combustion Institute 35 (2015) 905-912.